JOURNAL OF APPLIED CRYSTALLOGRAPHY
ISSN 1600-5767

# Crystal structure of Re-substituted lanthanum tungstate $La_{5.4}W_{1-y}Re_yO_{12-\delta}$ ($0 \leq y \leq 0.2$) studied by neutron diffraction

**Andrea Fantin,[a]* Tobias Scherb,[a] Janka Seeger,[b] Gerhard Schumacher,[a] Uta Gerhards,[c] Mariya E. Ivanova,[b] Wilhelm A. Meulenberg,[b] Roland Dittmeyer[c] and John Banhart[d]**

[a]Department of Microstructure and Residual Stress Analysis, Helmholtz-Zentrum Berlin für Materialien und Energie, GmbH, Hahn-Meitner-Platz 1, Berlin, 14109, Germany, [b]Institute of Energy and Climate Research, Forschungszentrum Jülich GmbH, Jülich, 52425, Germany, [c]Institute for Micro Process Engineering, Karlsruhe Institute of Technology, Hermann-von-Helmholtz-Platz 1, Eggenstein-Leopoldshafen, 76344, Germany, and [d]Department of Applied Materials, Helmholtz-Zentrum Berlin für Materialien und Energie GmbH, Hahn-Meitner-Platz 1, Berlin, 14109, Germany. *Correspondence e-mail: andrea.fantin@helmholtz-berlin.de

Received 17 March 2016
Accepted 15 July 2016

Edited by D. Pandey, Indian Institute of Technology (Banaras Hindu University), Varanasi, India

**Keywords:** Re-substituted lanthanum tungstates; $La_{5.6}WO_{12-\delta}$; anharmonic vibrations; anisotropic displacement parameters; mixed protonic electronic conductors; neutron diffraction.

**Supporting information**: this article has supporting information at journals.iucr.org/j

A precise determination of sample composition and water uptake of $La_{6-x}WO_{12-\delta}$ ($0.4 \leq x \leq 0.8$) and Re-substituted $La_{5.4}W_{1-y}Re_yO_{12-\delta}$ ($0 \leq y \leq 0.2$) lanthanum tungstate is carried out. Sample compositions and water uptake were determined by electron probe micro-analysis and thermogravimetry, respectively. A single-phase region of Re-substituted lanthanum tungstates is reported. The crystal structure of two selected specimens produced by the citrate-complexation route based on the Pechini method, namely $La_{5.4}WO_{12-\delta}$ and $La_{5.4}W_{0.8}Re_{0.2}O_{12-\delta}$, was investigated by neutron diffraction in the temperature range $1.5 \leq T \leq 1200$ K. The structural model for lanthanum tungstates is validated, according to which the Wyckoff site shared by La and W ($Fm\bar{3}m$ space group, 24*d* site) is split with half-site occupancies ($Fm\bar{3}m$ space group, 48*h* site). Replacement of W by up to 20 mol% Re does not change the lattice structure, and Re atoms substitute for W statistically in both 4*a* and 48*h* Wyckoff sites of the $Fm\bar{3}m$ space group, as shown by combining the average neutron scattering length procedure, thermogravimetry and electron probe micro-analysis. Using the Willis and Pryor approach to anisotropic displacement parameters it is shown that the remaining static disorder in the unit cell found in $La_{5.4}WO_{12-\delta}$ and $La_{5.4}W_{0.8}Re_{0.2}O_{12-\delta}$ structures is comparable, when the $Fm\bar{3}m$ space group with split 48*h* site is employed. Through the estimation of the Debye temperature for both compounds, extracted from the analysis of thermal expansion coefficients and from the Willis and Pryor approach, anion anharmonic vibrations like those in yttria-stabilized zirconia are proven to exist in LaWO for the first time.

## 1. Introduction

Hydrogen has the highest energy density amongst all fuels and has, therefore, been suggested for use as primary energy carrier, for example, in cars (Sorensen, 2007; Ho & Karri, 2011), buses (Genovese *et al.*, 2011), submarines (Kim *et al.*, 2008) and power plants (Niknam *et al.*, 2013; Wang *et al.*, 2013). Hydrogen gas can be produced through water electrolysis using renewable electrical energy or it can be obtained from fossil fuels, for example by steam reforming of natural gas. Whilst the former technology is the cleaner one, the latter is still economically more favourable, but produces hydrogen along with other gas impurities such as $H_2O$, $CO_x$, $NO_x$ and $SO_x$, which restricts its use as a fuel of high purity. Therefore, it is desirable to develop efficient technologies suitable for delivering highly pure $H_2$ out of a mixture of different gases and at the same time enabling one to control, collect and store

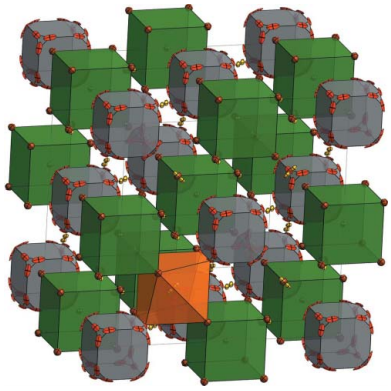

the other gas components separated during the process. New technologies to obtain pure hydrogen through gas separation are applicable using ceramic membranes as solid separators, which must have sufficiently high proton and electron bulk conductivity (good mixed conductors), giving a net $H_2$ flux across the membrane. Moreover, materials for hydrogen separation membranes should be chemically stable in the above-mentioned gas atmospheres, have high $H_2$ selectivity and activity at their surfaces, and be mechanically and thermally stable for long-term operation and elevated temperatures. While for most of these materials a choice between either good conductivity (perovskites with alkaline earth metal; Norby, 1999; Iwahara *et al.*, 1981; Iwahara, 1988) or stability [rare-earth sesquioxides (Haugsrud *et al.*, 2005), pyrochlores (Shimura *et al.*, 1996), acceptor-doped niobates (Haugsrud & Norby, 2006; Ivanova, Ricote *et al.*, 2012; Ivanova *et al.*, 2015; Palisaitis *et al.*, 2015)] has to be made, rare earth tungstates (LnWO) have been identified as appropriate candidates exhibiting both properties. As shown in recent studies, LnWO specimens with Ln = La (LWO) or Nd (NWO) exhibit conductivities comparable to those of the best perovskites (Meulenberg *et al.*, 2013; Escolastico, Seeger *et al.*, 2013; Seeger *et al.*, 2013) and excellent stability in acidic atmospheres (Escolástico *et al.*, 2012; Escolástico, Solís *et al.*, 2013; van Holt *et al.*, 2014). Replacement of W by the more reducible Re or Mo increases the electronic conductivity and leads, in the case of Re, to the highest values of $H_2$ permeation flow in the bulk at intermediate temperatures reported to date (Escolastico, Seeger *et al.*, 2013).

Besides the above-mentioned macroscopic material properties, the crystallographic structure of lanthanum tungstate (LWO) has frequently been investigated (Magrasó *et al.*, 2009, 2012, 2013; Haugsrud, 2007; Erdal *et al.*, 2012; Kalland *et al.*, 2013; Magrasó & Haugsrud, 2014). Subtle distortions in the LWO crystal lattice prevented a reliable determination of the crystal structure until very recently. The main problem was the discrepancy between the refined and the nominal stoichiometry. Specifically, around 20 mol% of W in the composition of the refined crystal structure was not allocated (Magrasó *et al.*, 2009). The first attempt to account for the tungsten excess was made by Magrasó *et al.* (2009) by placing tungsten onto interstitial positions. Later, a definite formula for the dissolution of tungsten in one of the two lanthanum positions was reported independently by Scherb (2011) and later by Magrasó *et al.* (2012). Subsequently, investigations on a local scale by density functional theory (DFT) calculations and pair distribution function (PDF) analysis were presented (Kalland *et al.*, 2013), while studies on the average crystal structure were carried out by means of neutron diffraction on Ca-doped LWO (Magraso *et al.*, 2013). Those results confirmed that the 20 mol% of non-localized tungsten atoms occupy the lanthanum position, which exhibits a highly distorted environment and hence allows greater flexibility with regard to the replacement of the larger lanthanum atoms by the smaller tungsten atoms. Scherb *et al.* (2016) identified the local structure in the $Pa\overline{3}$ space group and quantitatively compared the average (by diffraction), medium-range (by PDF) and local (by PDF and EXAFS) crystal structures. They suggested a model of local order according to which the $Pa\overline{3}$ space group well describes the data up to about three unit cells (35 Å). Above this value, modelling with an average crystal structure ($Fm\overline{3}m$ space group) yielded better fit residuals.

The aim of this work is to analyse in detail the structure of Re-substituted LWO lanthanum tungstates. These compounds have been selected because of their high stability in acidic atmospheres and their high values of bulk-$H_2$ permeation flow. Re atoms enhance the overall conductivity owing to the increase of electronic charge carriers, which makes this compound more suitable for $H_2$-related technologies (Seeger *et al.*, 2013; Escolastico, Seeger *et al.*, 2013). A limit of Re solubility in lanthanum tungstate has been found by Seeger *et al.* (2013) and Escolastico, Seeger *et al.* (2013), and was estimated to be around 20 mol% replacement of W by Re [Re/(W + Re)], corresponding to about 3 wt%. Above this value, depending on the La/(W + Re) ratio, secondary phases form and a decrease in conductivity as well as a deterioration of mechanical and permeation properties was observed. Detailed information about the effects caused by secondary phases in LWO are given elsewhere (Ivanova, Seeger *et al.*, 2012; Seeger *et al.*, 2013; Magrasó *et al.*, 2009).

In the first part of this work, results from thermogravimetric (TG) measurements and electron probe micro-analysis (EPMA) are reported and linked with the outcome obtained by LeBail refinements of neutron diffraction data. Techniques such as TG and EPMA are required to obtain information on the water uptake and specimen composition, respectively. Such features affect diffraction results such as cell parameter and oxygen occupancies. For elucidating the structure they need to be thoroughly analysed. Elemental mapping was used to assess the state of homogeneity of investigated specimens.

The second part of this work contains an exhaustive analysis of the nonsubstituted sample LWO. In order to study and validate the structure of LWO, the models of Scherb (2011) and Magraso *et al.* (2013) were used to fit our datasets and compared with each other. The models of the average crystal structure presented by Scherb (2011) and Magraso *et al.* (2013) are similar but not identical. Examination of the structural details is required as the most reliable starting point is essential for characterizing successfully the structure of Re-substituted samples, the results of which are reported in the last part of the present work. Moreover, approaches by Housley & Hess (1966) and Willis & Pryor (1975), which allow one to derive the amount of remaining static disorder at $T \leq 5$ K, are applied to two specimens, namely the nonsubstituted and the highest Re-substituted (20 mol%) LWO, and the results are compared with each other. This comparison enables one to evaluate the validity of the structural models and provides a quantitative value of the unmodelled static disorder. Finally, the second free parameter given by the Willis & Pryor (1975) model is the Debye temperature $T_D$. The value of $T_D$ extracted from the fit is compared with the one estimated from the cell parameters as obtained from refinements on neutron diffraction patterns as a function of temperature. Substantial discrepancies of the $T_D$ values found lead to the

conclusion that anion anharmonic vibrations in LWO exist, as discussed in the final part of this work.

## 2. Experimental

### 2.1. Samples

**2.1.1. Synthesis**. Powders of the sample series $La_{6-x}WO_{12-\delta}$ ($0.4 \leq x \leq 0.8$) were prepared *via* solid state reaction. In $La_{6-x}WO_{12-\delta}$, $x$ and $\delta$ represent the deviations from the stoichiometry of the material family $Ln_6WO_{12}$ (Ln = rare earth) reported in the 1960s and 1970s (Yoshimura & Rouanet, 1976; Chang *et al.*, 1966; Chang & Phillips, 1964). Although it is possible to produce large amounts of powder *via* the conventional solid state reaction, its drawback lies in the limited diffusion of the reactants. This is especially the case when samples containing a low concentration of one or more atomic species are produced, as for the Re-substituted (<3 wt%) lanthanum tungstate. Therefore, the sample series $La_{5.4}W_{1-y}Re_yO_{12-\delta}$ ($0 \leq y \leq 0.2$) was prepared through the citrate-complexation route based on the Pechini reaction (Pechini, 1967). In $La_{5.4}W_{1-y}Re_yO_{12-\delta}$, $y$ represents the substitution on the W site by Re. The use of the solid state reaction process and the citrate-complexation route for the production of $La_{6-x}WO_{12-\delta}$ ($0.4 \leq x \leq 0.8$) and $La_{5.4}W_{1-y}Re_yO_{12-\delta}$ ($0 \leq y \leq 0.2$) are described in detail by Seeger *et al.* (2013). Before grinding of the sintered pellets into powders, polishing was carried out on the surfaces of each pellet, to remove eventual contaminations during sintering, and the surface was checked by conventional X-ray diffraction until no change of the patterns was observed.

**2.1.2. Pre-treatment: dry/wet specimens**. The samples were dried in a glass tube placed in a movable furnace. After evacuation of the glass tube and purging with argon gas twice, the samples were dried under a stream of argon gas in $Al_2O_3$ holders (50 × 20 × 20 mm) at 1173 K for 4 h. After the dry samples had been cooled down to room temperature, two bubble bottles filled with $D_2O$ were connected to the argon (Ar) or synthetic air (SA) pipe supplying the atmosphere to the furnace. The furnace was kept at 623 K for 5 h. Finally, the pre-treated powders were stored in glass holders which were filled with argon gas prior to transfer to the experimental stations.

**2.1.3. Notations used**. In the present work, samples labelled 'dry' or 'dry(Ar)' refer to samples dried under argon atmosphere. $D_2O$ humidification performed under a stream of argon gas and synthetic air are referred to as $D_2O$(Ar) and $D_2O$(SA), respectively. The label 'wet' or 'wet($D_2O$)' refers to both $D_2O$(Ar) and $D_2O$(SA) humidification pre-treatments. '*Ex situ*' and '*in situ*' mean that the specimen treatments under reducing or oxidizing atmospheres were performed prior to or during the experiment, respectively.

### 2.2. Methods

**2.2.1. Electron probe micro-analysis**. The composition of the specimens was measured by electron probe micro-analysis in a JEOL JXA 8530F field emission microprobe. Samples and reference ($La_2O_3$, $WO_3$ and $ReO_3$) materials were embedded in epoxy-resin holders (2.5 cm diameter), and the surface was covered with carbon by the evaporation process. For each specimen 15 measurements were performed in different specimen regions and grains to enhance the precision of the analysis. The following measurement specifications were used: voltage 20 kV; electron current 50 nA; beam diameter Ø 2 µm or 500 nm, depending on the grain size. Elemental maps were taken in a 45 × 45 µm region at the same voltage. Images of the specimens were recorded in the backscattered electron (BSE) mode prior to elemental map acquisition.

**2.2.2. Thermogravimetry**. A Netzsch TG209F1 Iris microbalance equipped with a mass spectrometer (QMS 403 Aëolos) was used for thermogravimetric measurements to determine the water uptake of the specimens during heating. $Al_2O_3$ sample holders were used for the TG measurements. The sample mass varied between 150 and 300 mg. Before measurement, the chamber was evacuated twice and then purged with a stream of 50 ml $min^{-1}$ argon gas for one hour, and subsequently heated at 10 K $min^{-1}$ from room temperature up to 1273 K.

**2.2.3. X-ray diffraction**. X-ray diffraction (XRD) was performed in Bragg–Brentano geometry with a Bruker D8 Advance instrument, equipped with a LYNXEYE detector and a nickel filter (0.5 µm). The characteristic radiation lines used were Cu $K\alpha_1$ (1.5406 Å) and Cu $K\alpha_2$ (1.5444 Å). Phase identification was carried out with the ICDD PDF2 database in the *EVA14* software (Bruker, 2008).

**2.2.4. Neutron diffraction**. A suitable technique to localize the position of Re atoms is neutron diffraction (ND). Re has been chosen to replace W and, hence, to distinguish these two atoms in the lattice is crucial for the accurate determination of the structure. Re has a coherent neutron scattering length about twice as large as that of W [$b_{coh}^{Re}$ = 9.2 (2) fm against $b_{coh}^{W}$ = 4.755 (18) fm], boosting the contrast between the two atomic species, which for X-rays is small owing to their similar atomic numbers ($Z_W$ = 74 and $Z_{Re}$ = 75). Concerning the other elements in the unit cell, La ($Z_{La}$ = 57) has a coherent neutron scattering length of 8.24 (4) fm whilst the neutron scattering length of oxygen ($Z_O$ = 8) is 5.805 (4) fm, providing enough contrast between the different kinds of atoms to locate the oxygen atoms in the structure. Overall, ND is an optimal technique to solve the structure of Re-substituted lanthanum tungstate. Moreover, as neutrons interact with atomic nuclei and are more sensitive to atomic displacements compared to X-rays, anisotropic displacement parameters (ADPs) can be determined much more accurately by ND than by XRD. ADPs could at first corroborate the structural model used and secondly discriminate whether in LWO the position shared by $La_2$ and $W_2$ is the 48*h* or the 24*d* Wyckoff site. To facilitate fit convergence and precision of the refinement, ND measurements were carried out in the low (<10 K) temperature range on two specimens prepared by the Pechini procedure: $La_{5.4}WO_{12-\delta}$ (labelled LWO_**P**, where **P** stands for Pechini) and $La_{5.4}W_{0.8}Re_{0.2}O_{12-\delta}$ (labelled Re20, where 20 denotes the nominal molar percentage of W replaced by Re). The former and the latter specimens have been selected amongst the

$La_{5.4}W_{1-y}Re_yO_{12-\delta}$ samples as the two boundary cases with no Re substitution ($y$ = 0, LWO_**P**) and with the highest Re concentration ($y$ = 20, Re20), respectively. This should facilitate the identification of Re atoms in the unit cell through comparison. Prior to the experiments, vanadium cans (6 mm diameter) were filled with the specimen powders in a glovebox under argon gas. ND measurements were performed at different experimental stations. LWO_**P** and Re20 specimens were measured at the high-resolution powder diffractometer D2B (Hewat & Heathman, 1984) at the Institute Laue–Langevin (ILL), at the powder diffractometer HRPT (Fischer *et al.*, 2000) at the Paul Scherrer Institute (PSI) and at the powder diffractometer FIREPOD (Tobbens *et al.*, 2001) at the neutron source BERII (Helmholtz-Zentrum Berlin). At D2B, the optimum wavelength of $\lambda$ = 1.594 Å and a cryo-cooler ($3.5 < T < 300$ K) were used. To improve resolution a small slit size and the central part of the detector (1/3 of the total height) were employed. The software *LAMP* (Richard *et al.*, 1996) at the experimental station was employed to treat the raw data. Diffractograms were recorded at $T$ = 5, 10, 30, 60, 100, 150, 200 and 298 K (D2B), and at $T$ = 1.5, 10, 100, 200 and 295 K (HRPT, $\lambda$ = 1.494 Å). At FIREPOD the optimum wavelength $\lambda$ = 1.79803 (2) Å was selected. A high-temperature furnace was used as sample environment to record patterns at $T$ = 298, 450, 600, 750, 900, 1050 and 1200 K. In this case, the vanadium cans were sealed (VCR metal gasket face seal fittings), preventing any oxygen loss. Depending on their pre-treatment, the LWO_**P** and Re20-wet($D_2O$) specimens were measured at D2B (ILL) or at HRPT (PSI), at the above-mentioned temperatures. The $D_2O$(Ar) samples were measured at D2B in a cryo-cooler, while the $D_2O$(SA) pre-treated specimens were measured at HRPT using an orange cryostat equipped with a four-sample changer stick. Neutron absorption in transmission geometry was taken into account, including $\mu R/\lambda$ values ($R$ is the can radius, *i.e.* $R$ = 0.3 cm). The packing density employed for calculating the absorption was 4 g cm$^{-3}$, estimated as 0.6 times the crystallographic density. The $\mu R/\lambda$ values vary between 0.027 and 0.032 Å$^{-1}$ depending on the wavelength and the specimen composition. The absorption corrections were kept fixed during the refinement procedure.

Structural refinements were carried out using the software *GSAS*, with the *EXPGUI* graphical user interface (Larson & Dreele, 2004), and *TOPAS* (Evans, 2010).

## 3. Results and discussion

### 3.1. Electron probe micro-analysis, thermogravimetry and LeBail refinements of neutron diffraction data

In Table 1, a résumé of the samples investigated in this work, along with the preparation methods, nominal and refined compositions, eventual secondary phases, techniques, and sample labels, is presented. Fig. 1 shows the La/(W + Re) ratios of the investigated specimens (Table 1) as a function of Re/(W + Re). The compositions of the $La_{5.4}W_{1-y}Re_yO_{12-\delta}$ ($0 \le y \le 0.2$) series measured with EPMA are indicated by green squares. The composition of the LWO series (open green squares) was determined through Vegard's law (Vegard, 1921) and scaled to the composition of LWO_**P** measured with EPMA, as explained below. Open red squares, instead, describe the calculated La/(W + Re) ratios which take into account the contribution of secondary phases found by XRD. For instance, the $La_2O_3$ phase contributes to the overall increase of the La/W ratio. Concerning the unsubstituted samples represented by open green squares, only the composition of specimen LWO_**P** was directly measured by EPMA. All other LWO specimens were scaled by the La/W ratio of LWO_**P** according to their lattice parameters in the dry condition.

As shown by Magrasó *et al.* (2009) and predicted by Vegard's law (Vegard, 1921), a linear behaviour of the lattice parameter as a function of the La/W ratio is expected, provided that identical preparation/sintering conditions are used (Seeger *et al.*, 2013) and that the substitution amount is low enough (Jacob *et al.*, 2007) to avoid high-order deviations (Chizmeshya *et al.*, 2003; Murphy *et al.*, 2010; Su *et al.*, 2012; Ganguly *et al.*, 1993; Li *et al.*, 2001). In the considered LWO system the substitution referred to is the replacement of less than 1 out of 24 La atoms (<5 at.%) per unit cell by a W atom. In this sense, Vegard's law should be approximately valid. Other examples of applying Vegard's law to ceramic systems can be found elsewhere (Rey & Muccillo, 2004; Schulze-Küppers *et al.*, 2015). DFT calculations (Kalland *et al.*, 2013) have shown that the oxygen vacancies in LWO have a slightly lower energy when occupying the 32*f* Wyckoff site of the

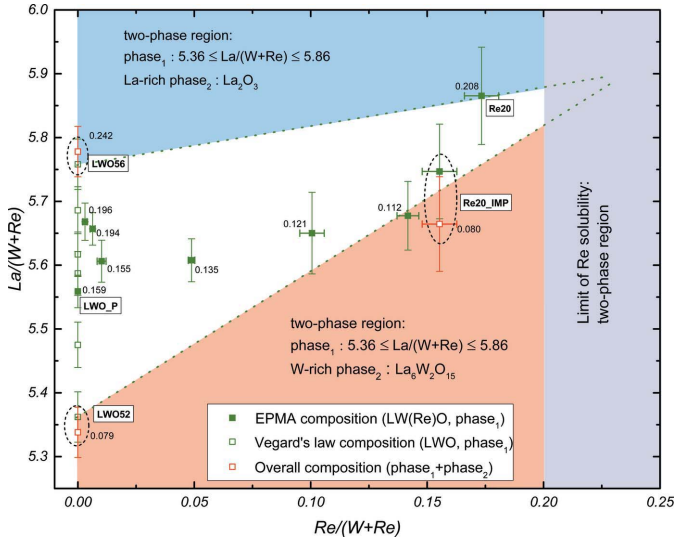


**Figure 1**
La/(W + Re) ratio as a function of replacement of W by Re [Re/(W + Re)]. The La/(W + Re) ratios described by green squares were determined by EPMA, the open green squares were determined through Vegard's law and comparison with LWO_**P** (*cf.* text), while the open red squares describe the La/W ratios modified according to secondary phase contributions indexed and quantified by XRD simulations. The white region between the green dotted lines represents the single-phase region of LW(Re)O specimens. The mass loss ($\Delta m$ in wt%, reported next to the squares) has been measured by TG on humidified [$D_2O$(Ar)] samples with an error of 0.005 wt%.

**Table 1**
Preparation method, nominal and experimental composition, phase composition status, techniques used, and sample labels as used throughout the manuscript.

| Sample series, preparation method nominal composition | Experimental (EPMA + XRD) overall composition | Secondary phases | Techniques used | Label of samples in the present work |
|---|---|---|---|---|
| $La_{6-x}WO_{12-\delta}$ ($0.4 \leq x \leq 0.8$) Solid state reaction | | | XRD, TG | LWO series |
| $La_{5.6}WO_{12-\delta}$ | $La_{5.81\ (4)}WO_{12-\delta}$ | $La_2O_3$ (<1 wt%) | | LWO56 |
| $La_{5.2}WO_{12-\delta}$ | $La_{5.33\ (4)}WO_{12-\delta}$ | $La_6W_2O_{15}$ (< 1 wt%) | | LWO52 |

| Sample series, preparation method nominal composition | Experimental (EPMA + XRD) overall composition | Secondary phases | Techniques used | Label of samples in the present work |
|---|---|---|---|---|
| $La_{5.4}W_{1-y}Re_yO_{12-\delta}$ ($0 \leq y \leq 0.2$) Pechini method | | | EPMA, XRD, TG | LW(Re)O, LW(Re)O series |
| $La_{5.4}WO_{12-\delta}$ | $La_{5.56\ (3)}WO_{12-\delta}$ | No | ND | LWO_**P** |
| $La_{5.4}W_{0.998}Re_{0.002}O_{12-\delta}$ | $La_{5.67\ (3)}W_{0.997\ (1)}Re_{0.003\ (1)}O_{12-\delta}$ | No | ND | Re02 |
| $La_{5.4}W_{0.995}Re_{0.005}O_{12-\delta}$ | $La_{5.66\ (3)}W_{0.994\ (1)}Re_{0.006\ (1)}O_{12-\delta}$ | No | ND | Re05 |
| $La_{5.4}W_{0.99}Re_{0.01}O_{12-\delta}$ | $La_{5.61\ (3)}W_{0.990\ (2)}Re_{0.010\ (2)}O_{12-\delta}$ | No | ND | Re1 |
| $La_{5.4}W_{0.95}Re_{0.05}O_{12-\delta}$ | $La_{5.61\ (3)}W_{0.951\ (2)}Re_{0.049\ (2)}O_{12-\delta}$ | No | ND | Re5 |
| $La_{5.4}W_{0.90}Re_{0.1}O_{12-\delta}$ | $La_{5.65\ (6)}W_{0.899\ (5)}Re_{0.101\ (5)}O_{12-\delta}$ | No | ND | Re10 |
| $La_{5.4}W_{0.85}Re_{0.15}O_{12-\delta}$ | $La_{5.67\ (5)}W_{0.858\ (5)}Re_{0.142\ (5)}O_{12-\delta}$ | No | ND | Re15 |
| $La_{5.4}W_{0.8}Re_{0.2}O_{12-\delta}$ | $La_{5.66\ (7)}W_{0.845\ (7)}Re_{0.155\ (7)}O_{12-\delta}$ | $La_6W_2O_{15}$ (<3 wt%) and Re-rich phase | | Re20_IMP |
| $La_{5.4}W_{0.8}Re_{0.2}O_{12-\delta}$ | $La_{5.86\ (7)}W_{0.826\ (7)}Re_{0.174\ (7)}O_{12-\delta}$ | No | ND | Re20 |

$Fm\bar{3}m$ space group and are bonded to the $La_1$ (4*b* Wyckoff) and $La_2/W_2$ (24*d* or 48*h* Wyckoff) sites. A higher concentration of La compared with W, therefore, results in a higher concentration of oxygen vacancies, which allows for a higher uptake of $D_2O$ into the lattice in the form of OD groups and D atoms after water splitting. This conclusion has been proven experimentally by Hancke *et al.* (2012, 2013), who have shown that a higher La/W ratio corresponds to a higher mass loss obtained from incorporated $H_2O$, *i.e.* in a higher concentration of oxygen vacancies. EPMA in combination with TG measurements as reported in Fig. 1 suggests the same behaviour for LWO and LW(Re)O specimens, where a higher $D_2O$ incorporation has been found with increasing La/(W + Re) content at fixed Re/(W + Re).

Furthermore, in order to obtain the same mass loss with increasing Re content, a shift to higher La/(W + Re) ratio is needed, which will be discussed at a later stage. An estimation of the single-phase region of LW(Re)O is reported in Fig. 1 (white region, delimited by green dotted lines). On the left side of Fig. 1, the single-phase region includes all the open green squares, beginning at La/W = 5.38 (4) (LWO52 open green square) and ending at La/W = 5.76 (4) (LWO56 open green square). On the right side of Fig. 1, owing to the lack of experimental data points, the single-phase region is restricted to Re/(W + Re) $\lesssim$ 0.20. The latter value denotes a limit of Re solubility in LWO (Escolastico, Seeger *et al.*, 2013; Seeger *et al.*, 2013). Secondary phases were found in some samples (Re20_IMP, LWO52, LWO56) by XRD, and their compositions were corrected (red squares in Fig. 1) accordingly as explained below. These phases were determined to be $La_6W_2O_{15}$ for data points within the orange region (Seeger *et al.*, 2013; Magrasó *et al.*, 2009; Ivanova, Seeger *et al.*, 2012) and to be $La_2O_3$ for data points within the blue region (Seeger *et al.*, 2013; Magrasó *et al.*, 2009; Ivanova, Seeger *et al.*, 2012), respectively below and above the single-phase region in Fig. 1. As an example, a BSE image of the impure sample Re20_IMP is reported and described in detail in the supporting information (Fig. S1). The EPMA measurements taken in the 5–20 µm sized grains yield a composition of $La_{5.74\ (7)}W_{0.85\ (1)}Re_{0.15\ (1)}O_{12-\delta}$, which is ascribed to the main phase present in the specimen, while the EPMA measurements in smaller grains (<2 µm) indicate an La/(W + Re) ratio of 3.5 (4), which is associated with the secondary phase $La_6W_2O_{15}$. Similar results are reported from scanning electron microscopy/energy dispersive X-ray spectroscopy measurements for samples of similar composition (Seeger *et al.*, 2013). No fingerprints of W-rich or La-rich secondary phases were observed in the LWO_**P** and Re20 specimens, whose elemental maps recorded by EPMA can be found in the supporting information (see Figs. S2 and S3).

All peaks of XRD patterns were indexed with the primary phase of the LWO series ($Fm\bar{3}m$, cubic) and a secondary phase $La_6W_2O_{15}$ ($C222_1$, orthorhombic) (Chambrier *et al.*, 2010; Ivanova, Seeger *et al.*, 2012) or $La_2O_3$ ($P\bar{3}m1$, hexagonal) (Schiller, 1986). This peak indexing implies no change of reflection conditions between the primary phases of the nonsubstituted and the Re-substituted lanthanum tungstates (see Fig. S4). A similar result has been reported by Amsif *et al.* (2012) and recently by Magraso & Frontera (2016), who studied the structure of LWO upon replacement of W by Mo. They did not find structure changes for <40 mol% Mo. Further structural details on Re-substituted lanthanum tungstate will be discussed in the second part of this work.

Rietveld refinement is expected to provide the amounts of different phases in Re20_IMP, LWO52 and LWO56 by using the integrated peak intensities of the diffraction patterns, from which the actual composition of the samples containing secondary phases can be inferred. However, all XRD data fits

failed when the crystal structure of the secondary phase given by the literature (Chambrier *et al.*, 2010; Schiller, 1986) was used. We, therefore, conclude that the amount of the secondary phase(s) is too low to be refined, as the peaks of the secondary phases with orthorhombic ($La_6W_2O_{15}$) or hexagonal ($La_2O_3$) space group are mostly hidden in the background. Nevertheless, the amount of secondary phase(s) was roughly estimated by XRD single peak fitting and pattern simulations, which resulted in a maximum amount of $La_6W_2O_{15}$ of 3 and 1 wt% for samples Re20_IMP and LWO52, respectively, and in a maximum amount of $La_2O_3$ of 1 wt% for sample LWO56. Considering the estimated amount of $La_6W_2O_{15}$, the La/(W + Re) ratio of sample Re20_IMP decreases from 5.74 (7) to 5.66 (7) (open red square Re20_IMP on the right-hand side in Fig. 1), while the La/W ratio for sample LWO52 decreases from 5.36 (4) to 5.34 (4) (open red square LWO52, bottom of Fig. 1). The values of $\Delta m$ obtained by TG for these two specimens (Re20_IMP, LWO52) are similar to each other ($\Delta m \simeq 0.08$ wt%). The mass losses of the Re20_IMP and LWO52 specimens are not influenced by the $La_6W_2O_{15}$ phase as the latter shows about the same value ($\Delta m \simeq 0.07$ wt%) and it is present only in a low amount (<3 wt%). For sample LWO56, in contrast, the presence of an La-rich phase ($La_2O_3$) increases the La/W ratio from 5.76 (4) to 5.78 (4) (open red square LWO56, top of Fig. 1). As $La_2O_3$ is highly hygroscopic, [$\Delta m \simeq 9.4$ wt% for $La_2O_3$-$D_2O$(Ar)] it contributes positively to the water uptake of the LWO56 specimen ($\Delta m = 0.241$ wt%) even in low amounts (<1 wt%). According to Fig. 1, the La/(W + Re) ratio increases with increasing Re content in order to maintain a constant amount of water uptake. This fact is ascribed to a decrease of the vacancy concentration with increasing Re substitution on the W site. This can be inferred by recalling the defect chemistry of LWO specimens according to the literature (Magrasó *et al.*, 2012; Hancke *et al.*, 2012, 2013; Erdal *et al.*, 2012). It is reported that for the nonsubstituted LWO an effective positive charge of +3 is carried by the tungsten donors substituted on lanthanum $La_2$ positions ($W_{La2}^{\bullet\bullet\bullet}$ in Kröger–Vink notation). The general chemical formulation for LWO is found to be

$$La_{28-x}W_{4+x}O_{54+\delta}v_{2-\delta}, \qquad (1)$$

where $\delta = 3x/2$ and $v$ denotes the number of vacancies per unit cell. According to Magrasó *et al.* (2012), $\delta$ defines the content of oxygen that compensates the $W_{La2}^{\bullet\bullet\bullet}$ donors, which we define as $\delta_W = 3x_W/2$. Escolastico, Seeger *et al.* (2013) reported that in the as-sintered or oxidized state the LW(Re)O system could contain $Re^{7+}$ and $Re^{6+}$ cations. As humidification under $D_2O$(Ar) has been performed, it is assumed that most of the Re is oxidized and in its +7 state. Re substitution for W on the $La_2$ position would result in $Re_{La2}^{\bullet\bullet\bullet\bullet}$ and hence, by charge compensation, in $\delta_{Re} = 4x_{Re}/2$. This means that more $Re^{7+}$ replacing $W^{6+}$ on the $La_2$ site would result theoretically in lower vacancy concentration ($v_{Re} < v_W$), which explains the decreasing hydration trend with increasing Re concentration reported in Fig. 1. In the literature a lower hydration effect in conductivity measurements for Re-substituted lanthanum tungstates has been observed (Seeger *et al.*, 2013). This statement will be confirmed in the discussion of the crystal structure.

Fig. 2 shows the temperature dependence of the lattice parameter in the dry (filled symbols) and wet($D_2O$) (open symbols) condition of LWO_**P** (red circles) and Re20 (green triangles).

In Fig. 2, it is seen that the lattice parameter of Re20 at any temperature and for both dry and wet($D_2O$) states is larger than that of LWO_**P**. The average difference between the wet($D_2O$) and dry states is a factor of two larger for Re20. If the oxidized state is assumed, this change in lattice parameter is opposite to what is expected from the ionic radii $R_i$ of Re and W. In this case $R_i(\mathrm{Re})_{6\mathrm{fold}}^{7+,6+} < R_i(\mathrm{W})_{6\mathrm{fold}}^{6+} = 0.60$ Å (Shannon, 1976), suggesting a decrease in lattice parameter through the replacement of W by Re. Under reducing conditions, Re oxidation states between +4 and +7 were observed in Re-substituted NWO compounds by X-ray photoelectron spectroscopy (Escolástico *et al.*, 2014). If similar conditions for LW(Re)O-dry are assumed, as $R_i(\mathrm{Re})_{6\mathrm{fold}}^{4+} = 0.63$ Å $> 0.60$ Å $= R_i(\mathrm{W})_{6\mathrm{fold}}^{6+}$ but also $R_i(\mathrm{Re})_{6\mathrm{fold}}^{7+,6+,5+} < R_i(\mathrm{W})_{6\mathrm{fold}}^{6+} = 0.60$ Å, the Re20 lattice parameter values are expected to be close to those of LWO_**P**. As demonstrated in Fig. 1, these apparent contradictions are caused by the slight difference in the La/(W + Re) ratio between the two materials, namely La/(W + Re) = 5.86 for Re20 and La/W = 5.56 for LWO_**P**. Lanthanum in sevenfold coordination has an ionic radius of 1.10 Å, which is about two times the size of W or Re

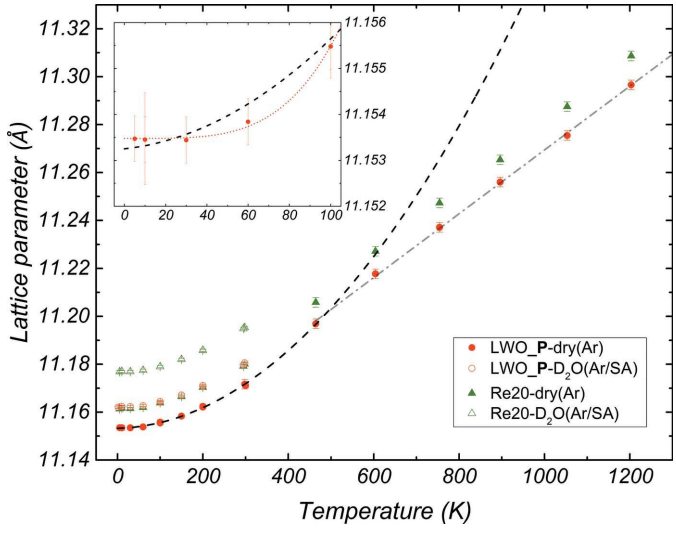


**Figure 2**
Temperature dependence of lattice parameters in the dry(Ar) (filled symbols) and $D_2O$(Ar/SA) (open symbols) condition of LWO_**P** (red circles) and Re20 (green triangles). Neutron diffractograms were collected at FIREPOD (BERII), D2B (ILL) and HRPT (PSI). Owing to small instrumental offsets, the lattice parameters have been scaled to values measured at ILL. The fit interpolations represent the temperature variation of LWO_**P**-dry(Ar) applying either a quadratic fit (black dashed line), to data points below 470 K, or a linear fit (grey dash–dotted line), above 470 K. In the inset, a magnification of the low-temperature region ($0 < T < 105$ K) of the LWO_**P**-dry(Ar) lattice parameter is presented, along with a magnification of the quadratic fit (black dashed line). Additionally, the best fit of the lattice parameter in the range $0 < T < 105$ K obtained by applying the Debye model [$a(T) = A + BT^4$, *cf.* text] is shown by the red dotted line.

ions, irrespective of their oxidation states. Therefore, a higher La/(W + Re) ratio results in a larger lattice parameter. A higher lanthanum content also leads to the larger lattice expansion of Re20 upon deuteration compared to LWO_**P**. A second confirmation that Re20 has a higher La/(W + Re) content than LWO_**P** arises from the comparison between the lattice parameter in the $D_2O$(Ar) state of Re20 [$a$ = 11.1972 (1) Å] and LWO56 [$a$ = 11.1920 (1) Å]. Data were taken by XRD and both patterns were fitted using the LeBail algorithm. The higher lattice parameter of Re20 compared to that of LWO56 is compatible with the higher La/(W + Re) ratio for Re20 compared to LWO56 found with EPMA and Vegard's law. Despite the same nominal composition (Table 1), the reasons for the minor differences in La/(W + Re) ratio of LWO_**P** and Re20 are ascribed to evaporation of W during sample synthesis (Amsif *et al.*, 2012; Escolástico *et al.*, 2014) and/or to segregation of W-rich phases at the specimen surface, which subsequently have been completely removed by polishing of the specimen.

For each specimen under both the dry and wet condition, the temperature dependence follows well a second-order polynomial [$R^2$ = 0.999, $a(T) = C + DT + ET^2$, with $C$, $D$, $E$ constant] below 470 K, given by the black dashed line for the LWO_**P**-dry(Ar) specimen taken as a representative example in Fig. 2. Above 470 K, for the two dry samples measured (LWO_**P** and Re20), linear regression fits describe the data well. The grey dash–dotted line represents the fit to the data of LWO_**P**-dry(Ar). This is in line with most compounds, where in the high-temperature region $T > T_D$ the lattice parameter expansion is linear with temperature, fulfilling the Dulong–Petit law [see equation (13) for details]. On the other hand, in the low-temperature region (Fig. 2 inset) the quadratic fit (black dashed line) does not describe the behaviour of the lattice parameter adequately. According to the Debye theory, the specific heat capacity at constant volume, $c_v$, is proportional to $T^3$ for low temperatures. Under certain approximations of the Grüneisen relation, the temperature dependence of the lattice parameter $a(T)$ is given by a simple integration of $c_v$ [see equations (11)–(13) for a detailed analysis]. Hence, in the temperature region shown in the inset $a(T)$ should be approximately proportional to $T^4$, provided that LWO does not behave as a metal at such temperatures. According to Debye theory, the $T^4$ interpolation $a(T) = A + BT^4$, where $A$ and $B$ are constant (see red dotted line in the inset), gives better residuals ($R^2$ = 0.995) for LWO_**P** than the $T^2$ interpolation $a(T) = F + GT^2$ ($R^2$ = 0.969, $F$ and $G$ are constant) performed in the same temperature range (results not shown here).

### 3.2. Crystal structure of LWO_P ($La_{5.56}WO_{12-\delta}$)

The LWO_**P** sample has approximately the same composition as the $La_{5.65}WO_{12-\delta}$ specimen used by Magraso *et al.* (2013) and was treated under similar conditions: the same sintering temperature (1773 K in air), comparable La/W ratio [from 5.56 (3) to 5.65 (4)] and similar experimental conditions [dry argon, *ex situ* 1173 K for LWO_**P**, *in situ* 1073 to 423 K for the specimen $La_{5.65}WO_{12-\delta}$ of Magraso *et al.* (2013)]. Scherb *et al.* (2016) reported a similar ratio to the present one, namely La/W = 5.57 (3) for an LWO specimen treated under dry argon, *ex situ* at 1173 K, but lower sintering temperature (1673 K in air). As shown in the literature (Magrasó *et al.*, 2009; Seeger *et al.*, 2013), the main structure-related effect of lower sintering temperature could be small remainders of secondary phases. Hence, we assume that the structure of the three specimens considered is equivalent.

The ND patterns taken on LWO_**P**-dry(Ar) were analysed in the following way. The final models of Magraso *et al.* (2013) and Scherb *et al.* (2016) were used to fit our datasets, as the two models proposed are similar but not identical. For instance, $La_2$ and $W_2$ atoms are reported to occupy the 24*d* Wyckoff site ($Fm\bar{3}m$ space group; Magraso *et al.*, 2013) or the 48*h* Wyckoff site with half occupancies ($Fm\bar{3}m$ space group; Scherb *et al.*, 2016). Another unclear point is that Magraso *et al.* (2013) reported negative ADPs for $W_2$ (ADPs not constrained with $La_2$) and for the oxygen atoms sitting on the 96*k* Wyckoff site, whose occupancy is the only one refined. In order to obtain the best structural model for the analysis of the Re-substituted specimens and also to rule out structural inconsistencies in LWO specimens, a thorough study on the refined ADPs as a function of temperature is presented. Refinements using both models have been performed, constraining $La_2$ and $W_2$ coordinates and ADPs to be the same, and constraining $La_2/W_2$ site occupancies in such a way that the 24*d* (Magraso *et al.*, 2013) or 48*h* (Scherb *et al.*, 2016) Wyckoff site shows full or half-site occupancy, respectively. At the final stage of the refinements, all the structural parameters were released to vary for the lowest temperature ($T$ = 5 K) in both cases to minimize thermal vibrations and the correlation between ADPs and site occupancies. Subsequently, all the site occupancy values found at $T$ = 5 K were fixed for all the other refined datasets collected at higher temperatures.

In Fig. 3, a comparison of the anisotropic displacement parameters obtained by applying the models of Magraso *et al.* (2013) and Scherb *et al.* (2016) to our data taken at $T \leq 298$ K is shown as a function of the temperature. Data points taken from Magraso *et al.* (2013) above 298 K are also added. As an indication of the overlapping region between the results of this work and the results of Magraso *et al.* (2013), $T$ = 298 K is represented by a brown vertical dashed line. In Fig. 3(*a*), the diagonal terms of the ADP tensor of the $O_1$ (96*k*) and $O_2$ (32*f*) atoms are depicted. The data for $T \leq 298$ K fitted with the model of Magraso *et al.* (2013) (open symbols) or the model of Scherb *et al.* (2016) (filled symbols) give similar results with respect to oxygen ADP values. Good agreement is also achieved in the overlapping region of the two datasets at $T$ = 298 K, irrespective of the model used. However, although the two models show the same behaviour of oxygen ADP values (Fig. 3*a*), it has to be pointed out that the ADP tensor orthogonalization gives non-positive-definite displacement ellipsoids of the $O_1$ 96*k* Wyckoff site for all the refinements using the model of Magraso *et al.* (2013), in accordance with the results of Magraso *et al.* (2013). On the other hand, considering the cation anisotropic displacements (Fig. 3*b*), the

fits performed with the models of Magraso *et al.* (2013) and Scherb *et al.* (2016) yield different results in two cases: (i) the $La_1U_{xx}$ and (ii) the $La_2/W_2U_{22/33}$ ADP terms, where $U_{xx}$ ($x = 1$, 2, 3) are the diagonal elements of the symmetric anisotropic tensor matrix (values given in Å$^2$). $U$ is related to the mean atomic displacements *via* $U = \langle u^2 \rangle$.

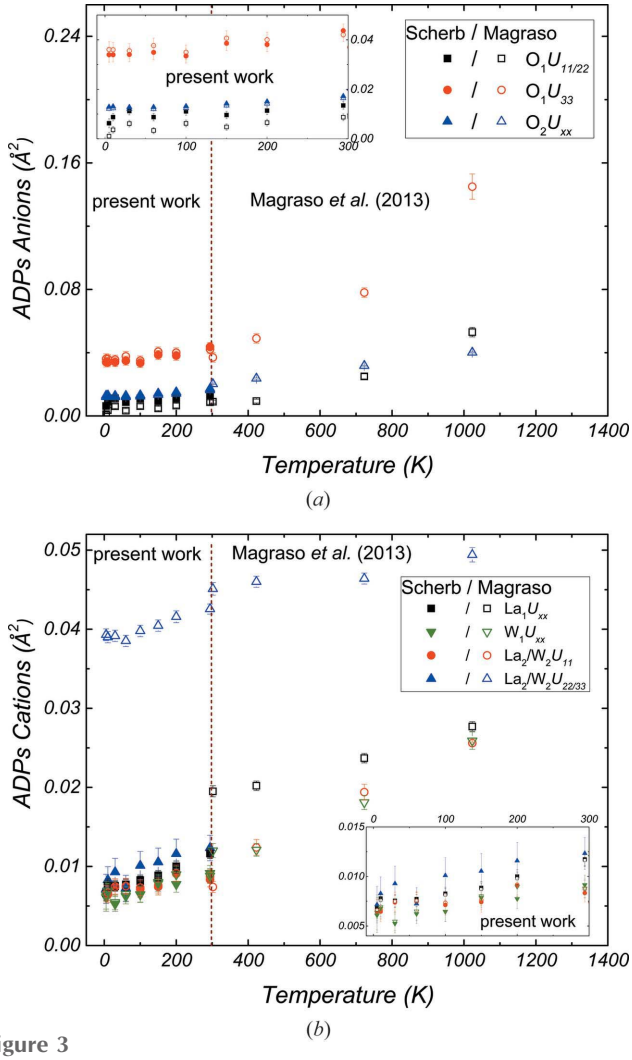


**Figure 3**
Temperature dependence of the anisotropic atomic displacement parameters of the LWO_**P**-dry(Ar) specimen, anions (*a*) and cations (*b*). Measurements between 5 and 298 K were performed at ILL (labelled as present work) and refined with $Fm\bar{3}m$ space group, using Scherb's model [Scherb *et al.* (2016), filled symbols] and Magraso's model [Magraso *et al.* (2013), open symbols]. A magnification of the results between $T = 5$ K and $T = 300$ K is shown in the corresponding insets. Above $T = 298$ K, indicated with a brown dashed line, the results taken from Magraso *et al.* (2013) are added [open symbols, region labelled as Magraso *et al.* (2013)]. The data point at $T = 298$ K of Magraso *et al.* (2013) is shifted to $T = 302$ K, while the data point of the present work at $T = 298$ K is shifted to $T = 294$ K for better visualization. $U_{xy}$ ($x, y = 1, 2, 3$; $x \neq y$) are not shown because they are rotations around the $xyz$ axes and in orthogonal systems they do not contribute to the length of the principal axes of the thermal ellipsoids (*cf.* text and literature; Massa, 2004; Fischer & Tillmanns, 1988). In (*a*), the values shown in open black squares (denoted as $O_1U_{11/22}$ Magraso in the figure) are not physical (*cf.* text). In (*b*), $W_2$ diagonal ADP values at $T = 423$ K, $T = 723$ K, $T = 1050$ K taken from Magraso *et al.* (2013) are not depicted because they are located outside the represented range ($W_2U_{22/33}$, $W_2U_{11}$) and negative ($W_2U_{11}$).

Concerning the $La_1$ atom, there is a discontinuity of the $U_{xx}$ values of the ADP term between the dataset of LWO_**P** ($T \leq$ 298 K) and the dataset of Magraso *et al.* (2013) ($T \geq 298$ K) in the overlapping region at $T = 298$ K, with the value reported by Magraso *et al.* (2013) being about twice as large as the value found in the present work. This discrepancy in the values of $La_1U_{xx}$ could be due to non-equivalent occupancies, which influence the displacement parameters, or due to different types of data acquisition [time-of-flight measurements in the work of Magraso *et al.* (2013) and measurements at constant wavelength in the present work]. For a detailed comparison between different instruments and methods of data collection the reader is referred to Hill & Cranswick (1994).

On the other hand, the difference in $U_{22/33}$ ADP values of $La_2/W_2$ is more relevant, being an order of magnitude higher and constant in the whole temperature range when the model of Magraso *et al.* (2013) is used. This can be explained as follows: when the $La_2/W_2$ atom is located on a 24*d* Wyckoff site (0, 0.25, 0.25) the different orientations of the $W_1$–$O_1$ octahedra situated at (0, 0, 0 – $x$, $x$, $z$) and (0, 0.5, 0.5 – $x$, $x$, $z$) result in a net electrostatic force applied by the $O_1$ atoms onto the $La_2/W_2$ atom (Scherb *et al.*, 2016). This net electrostatic force is applied to the $La_2/W_2$ atom along the diagonal ($yz$ direction) between the two octahedra, *i.e.* either towards the $W_1$–$O_1$ octahedron centred at (0, 0, 0) or towards the $W_1$–$O_1$ octahedron centred at (0, 0.5, 0.5). In turn, the $La_2/W_2$ atom is pulled either to (0, 0, 0) or to (0, 0.5, 0.5), which explains the splitting of the $La_2/W_2$ site. This accounts for the high values of the $U_{22/33}$ terms in the model of Magraso *et al.* (2013). The two major inconsistencies reported above for the model of Magraso *et al.* (2013), one for the anions (non-positive displacement ellipsoids for the 96*k* oxygen site) and one for the cations [the high $U_{22/33}$ ADP term of $La_2/W_2$; see Fig. 3(*b*)], are correlated and express the same aspect. The $La_2/W_2U_{22/33}$ displacement parameter is elongated towards the 96*k* $O_1$ sites and decreases the 96*k* $O_1$ displacement parameters in such a way that the 96*k* $O_1$ orthogonalized ADP in the direction towards the 24*d* site ($U_{11/22}$) becomes negative.

As pointed out, for example, by Massa (2004), the off-diagonal terms of the ADP tensor $U_{xy}$ ($x, y = 1, 2, 3$; $x \neq y$) refer to the orientation of the displacement ellipsoid with respect to that of the reciprocal cell axes. In non-orthogonal systems, they also have a component related to the lengths of the principal ellipsoid axes. For detailed information see Fischer & Tillmanns (1988). They state that the orthogonalization of the ADP's tensor should give positive values in the diagonal to obtain a complete set of physically meaningful ADPs. In other words, before using any ADP values, the three eigenvalues of the anisotropic tensor (which correspond to the reciprocals of the squares of the ellipsoid's semi-axes) have to be positive definite. As the LWO_**P** structure is represented by a cubic ($Fm\bar{3}m$) space group, the off-diagonal terms related to $La_2/W_2$, $O_1$ and $O_2$ are not shown in Fig. 3, but they are reported in the supporting information along with all the refinement results of the LWO_**P**-dry(Ar) specimen in the whole range of temperatures and for the structural models of both Scherb *et al.* (2016) and Magraso *et al.* (2013). In

Tables S1–S16 given in the supporting information, the ADP values marked in red show when the orthogonalization of the ADP tensor into positive-definite eigenvalues is not fulfilled.

From Fig. 3, it can be noticed how the extrapolation of anisotropic displacement parameters to $T$ = 0 K does not appear to be satisfied for almost all ADPs independently of the model used. It is known that the relationship between thermally induced mean-square atomic displacements and temperature is not linear and that vibrations persist even at $T$ = 0 K. Thus, for any chosen temperature, the displacement parameter is a combination of a static and a temperature-dependent term, which reflects dynamic disorder:

$$B_k(T) = B_k^{\rm thermal}(T) + B_k^{\rm static}, \qquad (2)$$

where $B_k$ is the displacement parameter of atom $k$ and $B_k$ is proportional to the mean square atomic displacement $u^2$ with $B = 8\pi^2u^2$. $T$ is the absolute temperature.

In order to estimate the maximum thermal contribution of the mean square atomic displacements at $T$ = 0 K the approach of Housley & Hess (1966) was adopted. With this approach, the minimum static component of the refined atomic displacements was determined. This procedure has also been used for the determination of static disorder in Cs hollandites (Cheary, 1991) and $ZrO_2$ (Argyriou, 1994). Expressing $B_k$ as a function of the normal mode frequencies, Housley & Hess (1966) state the following upper limit of the temperature-dependent term:

$$\left[B_k^{\rm thermal}(T = 0\,{\rm K})\right]^2_{\rm max} \leq \frac{h^2}{2m_k k_{\rm B} T} B_k(T), \qquad (3)$$

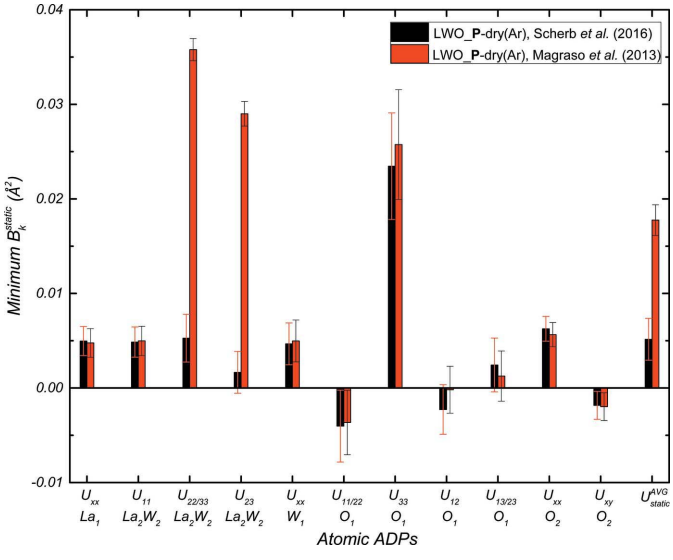


**Figure 4**
Minimum static disorder according to the approach of Housley & Hess (1966) obtained for the models of Scherb *et al.* (2016) (black bars) and Magraso *et al.* (2013) (red bars), applied to LWO_**P**-dry(Ar) and calculated at $T$ = 5 K. Each atom and all of its anisotropic displacement parameters are included. The last column represents the weight-averaged minimum static disorder in the unit cell, *i.e.* $U^{\rm AVG}_{\rm static} = [1/(8\pi^2 M)] \times \sum_k^{\rm cell} m_k B_k$, where $M = \sum_k^{\rm cell} m_k$ is the sum of the masses $m_k$ of each atom $k$ in the unit cell.

where $h$ and $k_{\rm B}$ are Planck's and Boltzmann's constants, respectively, and $m_k$ is the mass of atom $k$. The equality in relation (3) holds true for high temperatures. The maximum thermal values of all anisotropic displacement parameters were calculated according to equation (3) at the highest-temperature data available measured with the same instrument and under the same conditions, *i.e.* at $T$ = 298 K, for both models. By subtracting $B_k^{\rm thermal}(T = 0\,{\rm K})_{\rm max}$ from the refined ADP values at the lowest experimental temperature, $B_k(T = 5\,{\rm K})$, the minimum value of the static disorder contribution, $B_k^{\rm static}$, was determined. The results obtained with the approach of Housley & Hess (1966) are plotted in Fig. 4.

As the Housley & Hess (1966) approach calculates the minimum $B_k^{\rm static}$, the actual values of $B_k^{\rm static}$ could be higher than the ones shown in Fig. 4. Before drawing any conclusion on the negative minimum $B_k^{\rm static}$ shown in Fig. 4, *e.g.* for the $O_1U_{11/22}$ ADP value, it has to be pointed out that only two values of $B_k(T)$ are considered in equations (2) and (3) and that the ADP tensor is not orthogonalized. The two values used, $B_k(T$ = 298 K) and $B_k(T$ = 5 K), induce uncertainties in the values shown in Fig. 4, while the non-orthogonalized ADP tensor could mislead the reader to think about actual negative displacement parameters.

The effect of constant and high ADP values in 24*d* Wyckoff sites in the model of Magraso *et al.* (2013) is seen in Fig. 4, according to which the minimum static disorder of all positions, with the exception of $La_2/W_2$ atoms, in the $U_{22/33}$ (and rotation $U_{23}$) terms is the same for the models of Magraso *et al.*

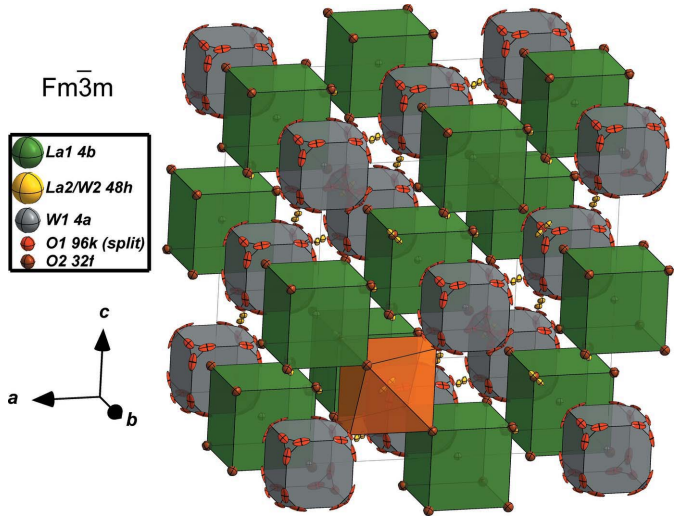


**Figure 5**
Average crystal structure of the LWO_**P**-dry(Ar) specimen with space group, atoms and Wyckoff sites as refined from the diffractogram collected at 5 K at ILL. Grey and green cubes represent W ($W_1$, 4*a* site) and La ($La_1$, 4*b* site) polyhedra, respectively. $W_1$ is sixfold coordinated by $O_1$ atoms (96*k* site partially occupied, red spheres). $La_1$ is eightfold coordinated by $O_2$ atoms (32*f* site almost fully occupied, brown spheres). The orange polyhedron denotes the $La_2/W_2$ shared and split 48*h* site. Locally, the $La_2/W_2$ site is sevenfold ($La_2$) or sixfold ($W_2$) coordinated by oxygen atoms owing to the different orientations of the neighbouring $W_1$–$O_1$ octahedra. However, the diffraction techniques average out the $W_1$–$O_1$ octahedra in cubes with oxygen partial occupancies. The shown ADPs represent 50% probability of finding an atom in the corresponding sphere/ellipsoid.

(2013) and Scherb *et al.* (2016). The inequality of the $La_2/W_2$ ADP values leads to a higher average unit cell static displacement of 0.018 (2) Å$^2$ for the model of Magraso *et al.* (2013) compared to 0.005 (2) Å$^2$ for the model of Scherb *et al.* (2016). The $O_1U_{33}$ ADP term also reflects static disorder independently of the model used and is caused by the different orientations of distorted $W_1$–$O_1$ octahedra in the unit cell, averaged in time and space. All other diagonal $U_{xx}$ ADPs have maximum values around 0.005 Å$^2$ (r.m.s. displacement value of about 0.07 Å) and indicate remaining static disorder in the refined structural model. However, their corresponding r.m.s. values are too low to improve the model significantly. Refinements using $La_1$ on 48*i*, $O_2$ on 96*k* and $O_1$ on 192*l* Wyckoff sites of the $Fm\bar{3}m$ space group were performed. The $F4\bar{3}m$ space group was also employed but relevant differences compared to the model of Scherb *et al.* (2016) were not observed. Finally, the structure of the LWO_**P**-dry(Ar) specimen is presented in Fig. 5 using the model of Scherb *et al.* (2016) and refinements of ND data collected at ILL at $T = 5$ K. Refinements on the LWO_**P**-$D_2O$(Ar/SA) specimens were performed in order to locate deuteron sites. However, owing to the low amount of D (0.44 $D_2O$ per unit cell) and the large size of one unit cell ($a^3 \simeq 1400$ Å$^3$), it was impossible to locate deuteron sites even for very low temperatures [$T = 5$ K (D2B), $T = 1.5$ K (HRPT)].

### 3.3. Crystal structure of Re20 ($La_{5.86}W_{0.83}Re_{0.17}O_{12-\delta}$)

The final structure of the nonsubstituted LWO_**P** shown in Fig. 5 was adopted as a starting point to characterize the structure of Re-substituted specimens. Three possible models for Re substitution on W positions within the $Fm\bar{3}m$ space group are considered: (i) Re occupies exclusively the 4*a* Wyckoff site (Model A), (ii) Re occupies exclusively the 48*h* Wyckoff site (Model B), and (iii) Re statistically occupies 4*a* and 48*h* Wyckoff sites (Model C) (see Fig. 5). Owing to the very different atomic radii of La [$R_i(\mathrm{La})^{8\mathrm{fold}}_{3+} = 1.16$ Å] and Re [$R_i(\mathrm{Re})^{6\mathrm{fold}}_{4+} = 0.63$ Å], Re substitution on the $La_1$ site was not considered.

The first approach to determine the structure of Re20 was to refine the site occupancies with a single atom per site, a procedure known as 'average neutron scattering length' (Furrer *et al.*, 2009; Stephan *et al.*, 2011), using the $Fm\bar{3}m$ space group. According to the refinement of the LWO_**P** sample, W atoms sit on 4*a* Wyckoff sites, whilst La occupies 4*b* and 48*h* Wyckoff sites. Vacancies on 4*a*, 4*b* and 48*h* Wyckoff sites are not considered. Refinements of occupancies within the average neutron scattering length approach have been performed for each dataset measured at the D2B beamline at ILL and at the HRPT beamline at the PSI for dry and $D_2O$ humidified specimens. The *TOPAS* program was used in order to refine simultaneously all the Re20 patterns for all temperatures. The $La_1$ occupancy was the only fixed parameter in the refinements. A fully occupied site has been assumed ($\mathrm{SOF}^{\mathrm{La_1}}_{4b} = 1$). The site occupancy factor parameter for each site was constrained to be the same for all temperatures and refined. The site occupancy factors have been assumed not to vary with temperature. While cations are not expected to diffuse in the structure in the temperature range measured, this approximation can be assumed also for the oxygen anions below $T = 298$ K, as no mass losses have been detected in the specimens with TG measurements below $T = 650$ K. The anion occupancies will be discussed at a later stage, whilst the results of the refinements for the cation sites are listed in Table 2. For comparison, the results of the refinements on the LWO_**P** specimen obtained through the neutron scattering length approach have also been added to Table 2. From Table 2 it is clear that not only W atoms occupy the 4*a* Wyckoff site, as its occupancy values are much larger than one. The refined coherent scattering length of the 4*a* position is $\overline{b}^{\mathrm{exp}}_{4a} = 5.41$ (2) fm, yielding an Re concentration on the 4*a* site of 0.147 (5). The same conclusion could be inferred for the 48*h* Wyckoff site after comparison between the average scattering occupancies of Re20 and LWO_**P** (Table 2) as the refined occupancy of the 48*h* site in LWO_**P** is 0.487 (2) compared to 0.491 (2) for Re20. However, owing to the higher La/(W + Re) ratio of Re20 [La/(W + Re) = 5.86] compared to the LWO_**P** specimen [La/(W + Re) = 5.56], the 48*h* average occupancy for Re20 could also reflect a higher La contribution. Because for each measured sample the 48*h* occupancies have in general La/(W + Re)-ratio-dependent La contributions that are difficult to isolate, the 4*a* site (shared only by Re and W) average scattering length has been studied for the whole LW(Re)O series.

**Table 2**
Refined site occupancy factors of Re20 4*a* and 48*h* cation sites, estimated through the average scattering approach, for one condition and all temperature datasets refined simultaneously.

The weighted average site occupancy factors for the Re20 specimen and, for comparison, for the LWO_**P** specimen are reported in the bottom rows. The weighting factor is the inverse square of the error associated with a single value.

| Conditions – instrument | $\mathrm{SOF}^{\mathrm{W}}_{4a}$ | $\mathrm{SOF}^{\mathrm{La_2}}_{48h}$ |
|---|---|---|
| Sample Re20 | | |
| Dry(Ar) – HRPT | 1.117 (10) | 0.486 (4) |
| $D_2O$(SA) – HRPT | 1.113 (9) | 0.493 (3) |
| Dry(Ar) – D2B | 1.178 (9) | 0.490 (5) |
| $D_2O$(Ar) – D2B | 1.138 (9) | 0.491 (3) |
| Average SOF | 1.138 (5) | 0.491 (2) |
| Sample LWO_**P** | | |
| Average SOF | 0.990 (5) | 0.487 (2) |

Refinements were performed with *TOPAS* in the same fashion as for Re20, *i.e.* obtaining the site occupancy factors after simultaneous refinements of patterns of the same specimen collected at different temperatures. It was assumed that the cation 4*a* site occupancy factor (SOF) is independent of the condition used; thus an average between the different conditions could be performed. The results reported in Fig. 6 are, therefore, the average of the SOFs for the 4*a* site for all the temperatures and all the conditions for the same specimen (green triangles). Moreover, a comparison of the average neutron scattering lengths considering the Re concentration determined with EPMA (Fig. 1) is presented in Fig. 6 (red dots).

The 4*a* site occupancies obtained by averaging the D2B and HRPT data deviate from the Re content measured by EPMA assuming only Re on the 4*a* site (filled red circles). Inconsistent results on Re1 and Re5 specimens have been found, ascribed to the low powder amount available. The corresponding data points have been marked with an asterisk and were not included in the linear fit performed (green dash–dotted line in Fig. 6). The deviation between the EPMA values and the refined values of $\overline{b}_{4a}^{\rm exp}$ increases with increasing Re concentration, suggesting that Re atoms do not occupy exclusively the 4*a* site. The deviations have been calculated to be about 15, 18 and 22% for Re20, Re15 and Re10, respectively. These values agree with a statistical replacement of W by Re, calculated for different La/(W + Re) ratios and depicted in Fig. 6 in grey lines. If a ratio of La/(W + Re) = 5.4 is considered, there are four W and one Re atoms per unit cell. Four atoms amongst them occupy the 4*a* site and the remaining one occupies the 48*h* site. If a statistical distribution is assumed, a deviation from the EPMA values of 20% for La/(W + Re) = 5.4 is expected, decreasing with increasing La/(W + Re) content to about 15% for La/(W + Re) = 5.86 (grey short-dashed line). By combining EPMA and ND measurements, it is therefore possible to place the missing Re concentration on the 48*h* Wyckoff sites. According to these results it can be confidently concluded that Re is statistically replacing W. Re occupies the 4*a* position, shared with W, but also resides on the 48*h* position, shared with both W and La. The above results from average scattering length refinements suggest that Model A and Model B can be excluded and Model C is most appropriate to describe the structure of Re20, with Re occupying both 4*a* and 48*h* Wyckoff sites. Finally, the refinement strategy for the Re20 specimen can be developed. As only two atoms (labelled $W_1$, $Re_1$) are sharing the 4*a* site, the starting occupancy values are set according to the average scattering length refinements, *i.e.* $\mathrm{SOF}_{4a}^{\rm W1} = 0.853$ and $\mathrm{SOF}_{4a}^{\rm Re1} = 0.147$, constrained to full site occupancy ($\mathrm{SOF}_{4a}^{\rm W1} + \mathrm{SOF}_{4a}^{\rm Re1} = 1$). In order to establish the starting values of the occupancies of the 48*h* Wyckoff site, another consideration has to be made. There are three atoms (labelled $La_2$, $W_2$, $Re_2$) which share the 48*h* Wyckoff site. From a computational point of view, only two equations (see below) are available to determine the three occupancies ($\mathrm{SOF}_{48h}^{\rm La2}$, $\mathrm{SOF}_{48h}^{\rm W2}$ and $\mathrm{SOF}_{48h}^{\rm Re2}$): one equation that assumes half-site occupancy of the 48*h* site,

$$\mathrm{SOF}_{48h}^{\rm La2} + \mathrm{SOF}_{48h}^{\rm W2} + \mathrm{SOF}_{48h}^{\rm Re2} = 0.5, \qquad (4)$$

and a second equation that considers the average scattering length $\overline{b}_{48h}^{\rm exp}$ calculated from Table 2,

$$\overline{b}_{48h}^{\rm exp} = \mathrm{SOF}_{48h}^{\rm La2} b_{\rm coh}^{\rm La} + \mathrm{SOF}_{48h}^{\rm W2} b_{\rm coh}^{\rm W} + \mathrm{SOF}_{48h}^{\rm Re2} b_{\rm coh}^{\rm Re} = 0.491 b_{\rm coh}^{\rm La}, \qquad (5)$$

where $\mathrm{SOF}_{48h}^{k2}$ and $b_{\rm coh}^{k}$ are, respectively, the occupancy of the 48*h* Wyckoff site and the neutron coherent scattering length of atom *k*.

The additional information for Rietveld refinement is provided by the EPMA measurements [La/(W + Re) = 5.86; see Fig. 1], which results in

$$\frac{\mathrm{La_{TOT}}}{\mathrm{W_{TOT}} + \mathrm{Re_{TOT}}} = \frac{48\,\mathrm{SOF}_{48h}^{\rm La2} + 4\,\mathrm{SOF}_{4b}^{\rm La1}}{48\left(\mathrm{SOF}_{48h}^{\rm W2} + \mathrm{SOF}_{48h}^{\rm Re2}\right) + 4\left(\mathrm{SOF}_{4a}^{\rm Re1} + \mathrm{SOF}_{4a}^{\rm W1}\right)} = 5.86, \qquad (6)$$

where $\mathrm{La_{TOT}}$, $\mathrm{W_{TOT}}$ and $\mathrm{Re_{TOT}}$ represent the total numbers of the corresponding atoms in one unit cell.

Equations (4)–(6) were used to determine the starting refinement occupancies $\mathrm{SOF}_{48h}^{\rm La2}$, $\mathrm{SOF}_{48h}^{\rm W2}$ and $\mathrm{SOF}_{48h}^{\rm Re2}$ for the 48*h* Wyckoff site. The three unknown parameters are $\mathrm{SOF}_{48h}^{\rm La2}$, $\mathrm{SOF}_{48h}^{\rm W2}$ and $\mathrm{SOF}_{48h}^{\rm Re2}$. The occupancy $\mathrm{SOF}_{4b}^{\rm La1}$ and the constrained sum of the occupancies $\mathrm{SOF}_{4a}^{\rm W1} + \mathrm{SOF}_{4a}^{\rm Re1}$ are set to unity, according to the assumptions made and to the refinements of LWO_**P** [$\langle \mathrm{SOF}_{4a}^{\rm W1} \rangle = 0.990$ (5), where $\langle\rangle$ denotes the weighted average; *cf.* Table 2]. The numerical factors on the left-hand side of equation (6) are the numbers of equivalent positions in the unit cell of the respective Wyckoff site (48 for the 48*h* and 4 for the 4*a* and 4*b* sites). The site occupancies calculated from equations (4)–(6) are $\mathrm{SOF}_{48h}^{\rm La2} = 0.486$ (1) and therefore $\mathrm{SOF}_{48h}^{\rm W2} + \mathrm{SOF}_{48h}^{\rm Re2} = 0.014$ (1). Owing to the low remaining amount of $W_2$ and $Re_2$ the starting values were set to $\mathrm{SOF}_{48h}^{\rm W2} = \mathrm{SOF}_{48h}^{\rm Re2} = 0.07$. In the refinements the occupancy $\mathrm{SOF}_{48h}^{\rm La2}$ was kept fixed to the value calculated ($\mathrm{SOF}_{48h}^{\rm La2} = 0.486$) until all other structural parameters (positions, ADPs, SOFs)

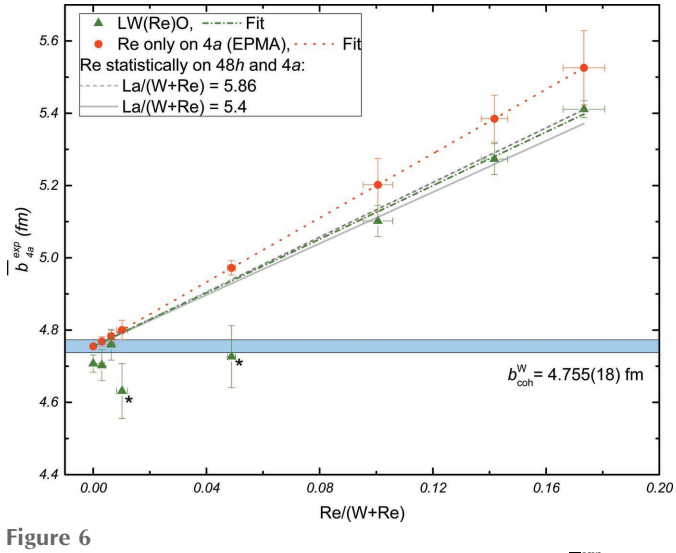


**Figure 6**
Average neutron scattering length of the 4*a*–$W_1$ Wyckoff site, $\overline{b}_{4a}^{\rm exp}$, for the LW(Re)O series, as a function of Re substitution for W [Re/(W + Re)]. Green symbols represent the average $\overline{b}_{4a}^{\rm exp}$ obtained from refinements performed on the LWO_**P**, Re02, Re05, Re1, Re10, Re15 and Re20-dry(Ar)/$D_2O$(SA) specimens at HRPT ($T$ = 1.5, 10, 100 and 295 K), on the Re1 and Re5-dry(Ar)/$D_2O$(Ar) specimens at D2B ($T$ = 298 K), on LWO_**P** at D2B ($T$ = 5, 10, 30, 60, 100, 150, 200 and 298 K), and on Re20 at D2B ($T$ = 5, 30, 60, 150, 200 and 298 K). The asterisks denote the data points not included in the fit (*cf.* text). Filled red circles show the 4*a* site occupancy calculated under the assumption that the Re amount measured by EPMA entirely occupies the 4*a* site. The grey lines show the 4*a* site occupancy assuming statistical distribution of Re for La/(W + Re) = 5.86 and La/(W + Re) = 5.4 in short-dashed and solid lines, respectively. The fit of $\overline{b}_{4a}^{\rm exp}$ is a straight line performed with direct *x* weighting [larger Re/(W + Re) weighs more] and with $\overline{b}_{4a}^{\rm exp}(0) = 1$ (4*a* fully occupied for the nonsubstituted LWO_**P**). The coherent scattering length of W is depicted in light blue.

**Table 3**
Fractional atomic coordinates, $x$, $y$, $z$, site occupancy factors, SOF, and equivalent and anisotropic displacement parameters, $U_{eq}$, $U_{xy}$, of Re20-$D_2O$(Ar) ($La_{5.86}W_{0.83}Re_{0.17}O_{12-\delta}$) from ND at $T$ = 5 K, refined with space group $Fm\bar{3}m$.

All the displacement parameters ($U_{eq}$, $U_{xx}$ and $U_{xy}$) are multiplied by a factor of 100. The lattice parameter and the residuals are also reported. The refined composition is $La_{27.3\,(1)}W_{3.8\,(3)}Re_{0.9\,(3)}O_{54.5\,(4)}$ [La/(W + Re) = 5.84, Re/(W + Re) = 0.187].

| Atom | Site | $x$ | $y$ | $z$ | $U_{eq}$ (Å$^2$) | SOF |
|---|---|---|---|---|---|---|
| $La_1$ | 4*b* | 0.5 | 0.5 | 0.5 | 0.82 | 0.990 (14) |
| $W_1$ | 4*a* | 0 | 0 | 0 | 0.36 | 0.854 (24) |
| $Re_1$ | 4*a* | 0 | 0 | 0 | 0.36 | 0.146 (24) |
| $La_2$ | 48*h* | 0 | 0.2355 (2) | 0.2355 (2) | 0.71 | 0.486 (2) |
| $W_2$ | 48*h* | 0 | 0.2355 (2) | 0.2355 (2) | 0.71 | 0.008 (5) |
| $Re_2$ | 48*h* | 0 | 0.2355 (2) | 0.2355 (2) | 0.71 | 0.006 (5) |
| $O_1$ | 96*k* | 0.1122 (2) | 0.1122 (2) | 0.0649 (3) | 1.57 | 0.245 (3) |
| $O_2$ | 32*f* | 0.3665 (1) | 0.3665 (1) | 0.3665 (1) | 1.36 | 0.967 (5) |

| Atom | $U_{11}$ (Å$^2$) | $U_{22}$ (Å$^2$) | $U_{33}$ (Å$^2$) | $U_{12}$ (Å$^2$) | $U_{13}$ (Å$^2$) | $U_{23}$ (Å$^2$) |
|---|---|---|---|---|---|---|
| $La_1$ | 0.82 (10) | 0.82 (10) | 0.82 (10) | | | |
| $W_1$, $Re_1$ | 0.36 (14) | 0.36 (14) | 0.36 (14) | | | |
| $La_2$, $W_2$, $Re_2$ | 0.67 (11) | 0.73 (16) | 0.73 (16) | | | 0.26 (14) |
| $O_1$ | 1.05 (17) | 1.05 (17) | 2.60 (25) | −0.19 (9) | −0.38 (10) | −0.38 (10) |
| $O_2$ | 1.36 (4) | 1.36 (4) | 1.36 (4) | 0.07 (4) | 0.07 (4) | 0.07 (4) |

| Lattice parameter (Å) | $T$ (K) | $R_{exp}$ (%) | $R_{wp}$ (%) | $\chi^2$ | $R_F^2$ (%) |
|---|---|---|---|---|---|
| 11.1770 (1) | 5 | 3.56 | 5.63 | 2.502 | 3.35 |

had reached convergence. Finally, $SOF_{48h}^{La2}$ was refined together with the other structural parameters and its value did not change. On the 48*h* site the parameters $SOF_{48h}^{W2}$ and $SOF_{48h}^{Re2}$ are constrained during the refinement by the condition $SOF_{48h}^{W2}$ + $SOF_{48h}^{Re2}$ = 0.014. In this way, the ratio La/(W + Re) was fixed and a discrimination between $W_2$ and $Re_2$ was possible. Anisotropic displacement parameters were also constrained and set equal for atoms occupying the same Wyckoff site.

As an example, the Re20-$D_2O$(Ar) refinement results are shown in Fig. 7 and Table 3, as the deuterated specimens could be refined with all the structural parameters simultaneously [contrarily to Re20-dry(Ar)]. In Fig. 7 and its insets, the ND pattern along with the corresponding calculated and difference intensities (Rietveld algorithm) is illustrated. The corresponding refined parameters are listed in Table 3.

Although the refinement of the ND pattern measured at $T$ = 5 K with all structural parameters free was possible only for the wet specimens, it has been found that the disorder of the cations in the dry(Ar) specimen is slightly higher than that in the wet specimen. This feature is ascribed to a higher vacancy concentration in the dry(Ar) specimen, in addition to Re reduction (see supporting information for cation ADPs; Fig. S5). This might be also the reason why the refinement of Re20-dry(Ar) patterns could not be finalized with coordinates, displacement parameters and occupancies refined at the same time. For completeness, the anion ADPs of Re20-dry(Ar)/$D_2O$(Ar) are also reported in the supporting information (Fig. S6).

Through the anion occupancies, information concerning the vacancy positions can be deduced. The occupancies have been taken from the refinement of the average neutron scattering length approach applied to the cations (see Table 2). As the anion sites are occupied only by oxygen atoms, the refined occupancy applying the average neutron scattering length approach is representative of the occupancy values refined with the appropriate structural model. In fact, the oxygen occupancy values from the final refinements (*cf.* Table 3) and the average neutron scattering length approach (Table 4) are comparable to each other. In Table 4, the refined occupancies of the anion sites are shown for Re20 and LWO_**P** specimens.

From Table 4, through the difference between dry(Ar) and wet($D_2O$) specimens measured at the same instrument, it is possible to infer where the vacancies might be located. Sample Re20 shows that at both experimental stations the refined occupancy of the 96*k* site of dry(Ar) and wet specimens is the same within the error and in the HRPT case is also comparable to the expected oxygen occupancy for the W–O octahedron ($SOF_{96k}^{O1}$ = 0.25 for octahedral $W^{6+}$). It can therefore be concluded that the $O_2$ (32*f*) site accommodates the vacancies. Here, the differences in the occupancies between the dry and the $D_2O$ conditions are

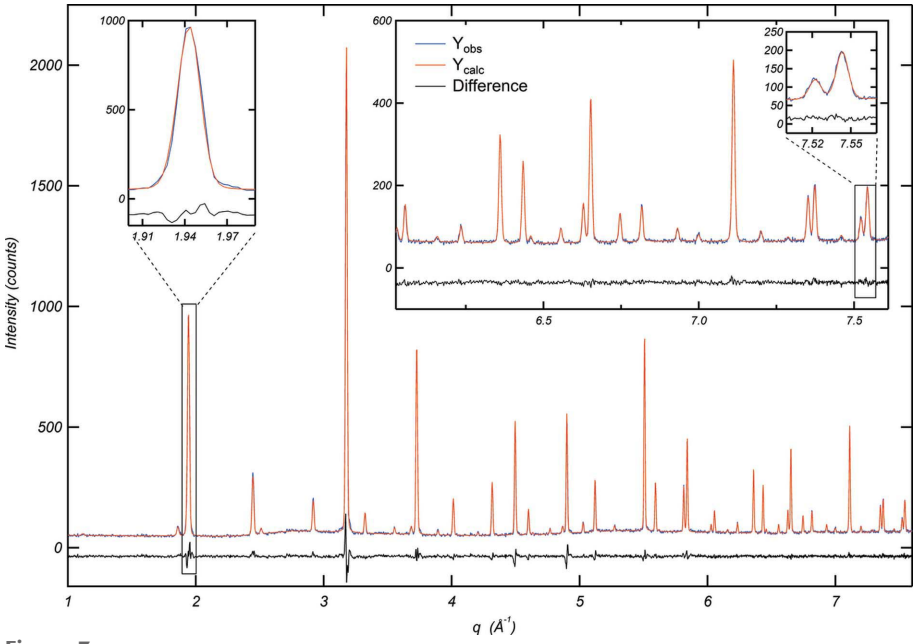


**Figure 7**
Neutron diffraction intensity plots of Re20-$D_2O$(Ar) ($La_{5.86}W_{0.826}Re_{0.174}O_{12-\delta}$) data collected at $T$ = 5 K at instrument D2B (ILL), as a function of the exchanged momentum $q$ (blue line), calculated data (red line) and difference of the two (black line). In the insets the high-$q$ data ($6 < q < 7.6$ Å$^{-1}$) are magnified, as well as three chosen diffraction peaks, one in the low-$q$ range and the last two in the high-$q$ range. In the insets, the difference line is shifted for better peak visualization.

Table 4
Refined anion site occupancy factors, SOF, of Re20 and LWO_**P** determined from the average neutron scattering approach, for all temperature datasets acquired at different conditions and instruments.

| | Sample Re20 | | Sample LWO_**P** | |
|---|---|---|---|---|
| Conditions – instrument | $SOF^{O1}_{96k}$ | $SOF^{O2}_{32f}$ | $SOF^{O1}_{96k}$ | $SOF^{O2}_{32f}$ |
| Dry(Ar) – HRPT | 0.250 (3) | 0.952 (9) | – | – |
| $D_2O$(SA) – HRPT | 0.250 (2) | 0.985 (6) | 0.247 (2) | 0.974 (6) |
| Dry(Ar) – D2B | 0.242 (2) | 0.949 (6) | 0.237 (2) | 0.930 (6) |
| $D_2O$(Ar) – D2B | 0.246 (2) | 0.977 (6) | 0.240 (2) | 0.964 (7) |

0.033 (15) and 0.028 (14) for HRPT and D2B, respectively. Higher oxygen occupancies in the LWO_**P** specimen are also found in the 32*f* Wyckoff site. However, the oxygen occupancies of the Re20 and LWO_**P**-dry(Ar) specimens measured at D2B give an overall oxygen amount in the unit cell slightly below the theoretical value. This could be ascribed to vacancy creation also on the 96*k* site, which gives an average coordination of $N$ = 5.69 (5) of W instead of $N$ = 6 for LWO_**P**-dry(Ar). Oxygen understoichiometry could derive from repeated dehydrations under reducing conditions which may alter the structure and eventually create vacancies also in the 96*k* Wyckoff site. However, as the oxygen atoms in 96*k* experience libration movements around W (Magraso *et al.*, 2013) and anharmonic vibrations (see discussion below), it remains difficult to establish whether these slight deviations from octahedral coordination of W are real or simply due to the disorder of 96*k* being inaccurately modelled. Nevertheless, from Table 4 it can be confidently stated that most of the vacancies in the specimens investigated are located on the 32*f* Wyckoff site. This statement is corroborated by the DFT calculations (Erdal *et al.*, 2012) for LWO.

### 3.4. Minimum static disorder and Debye temperature

In order to calculate the minimum static disorder for Re20, a second approach was used and applied to the LWO_**P** specimen for comparison. The cell-mass-weighted average displacement parameter $B_M$ has been estimated. $B_M$ represents the sum of cell-mass-weighted average temperature-dependent ($B_M^{thermal}$) and temperature-independent ($B_M^{static}$) displacement parameter terms. Willis & Pryor (1975) adapted the Debye model to the temperature-dependent term, $B_M^{thermal}$, in such a way that

$$B_M^{thermal}(T) = \frac{6gh^2}{Mk_B T_D}\left[\frac{\varphi(x)}{x} + \frac{1}{4}\right], \quad x = \frac{T_D}{T}, \tag{7}$$

where

$$B_M = (1/M)\sum_k m_k B_k, \tag{8}$$

and the summation is done over the unit cell, $h$ and $k_B$ are the Planck and Boltzmann constants, $M$ and $g$ are, respectively, the mass and the number of atoms in the unit cell, and $\varphi(x)$ is the Debye function, given by

$$\varphi(x) = \frac{1}{x}\int_0^x \frac{y}{\exp(y)-1}\,dy. \tag{9}$$

In summary, the refined anisotropic displacement parameters $B_k$, mass weighted over the unit cell, $B_M$, comply with the following expression (Cheary, 1991; Argyriou, 1994):

$$B_M(T) = B_M^{thermal}(T) + B_M^{static} = \frac{6gh^2}{MK_B T_D}\left[\frac{\varphi(x)}{x} + \frac{1}{4}\right] + B_M^{static}. \tag{10}$$

Equation (10) has two free parameters: $B_M^{static}$ and $T_D$.

The cell-weighted displacement parameter $B_M$ calculated from refinements of samples LWO_**P** and Re20 is represented in Fig. 8 along with the fits performed with equation (10). The values of $B_M^{static}$ obtained by equation (10) are then compared with those obtained from the Housley & Hess (1966) model. The values of $B_k^{static}$ were calculated as explained in §3.2 and were then averaged over the unit cell with equation (8). All the parameters determined in this way are listed in Table 5.

All the fits using the Willis & Pryor (1975) approach, partly shown in Fig. 8 (inset), represent the experimental data satisfactorily, and intercept $T$ = 0 K [$B_M^{static}(T = 0\,K)$] at about the same value. In general, a comparison between the absolute values of $B_M^{static}(T = 0\,K)$ is difficult, owing to the dependence of the ADPs on the background and the site occupancies. Nevertheless, slightly lower $B_M^{static}(T = 0\,K)$ absolute values have been found for Re20-wet($D_2O$) and LWO_**P**-wet($D_2O$), compared to the Re20-dry(Ar) and LWO_**P**-dry(Ar) specimens, respectively. This is in agreement with the higher ADP values for Re20-dry(Ar) compared to Re20-$D_2O$(Ar) and could be explained by higher vacancy concentration in addition to Re reduction, as mentioned previously. The lower

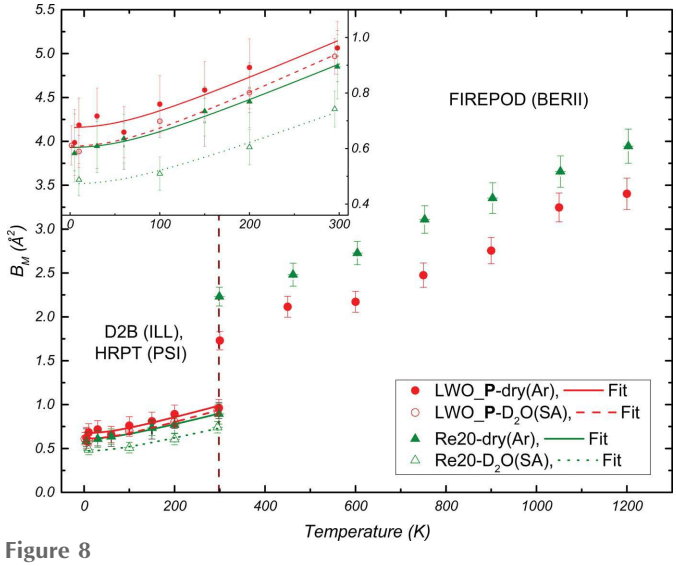


Figure 8
Cell-weighted displacement parameter $B_M$ from ND data as a function of temperature for samples LWO_**P**-dry(Ar) and $D_2O$(SA), and Re20-dry(Ar) and $D_2O$(SA), fitted with equation (10) for $T \leq 298$ K (see inset). Below and above $T$ = 298 K (brown dashed line) the results from D2B(ILL)/HRPT(PSI) and FIREPOD(BERII) ND data, respectively, are reported.

**Table 5**
Cell-weighted minimum static disorder parameters [$B_M^{static}(T = 0\,K)$], obtained from the two different approaches of Housley & Hess (1966) and Willis & Pryor (1975).

Values for the Debye temperature $T_D$ are also listed, fitted with the Willis & Pryor (1975) approach and derived from the TEC, respectively. For the Re20 and LWO_**P** specimens, all pre-treatments were used in the same TEC dataset and hence only one $T_D$ is derived. Averages are the weighted mean, where the weighting factor is the inverse square of the error associated with the single values.

| | Housley & Hess | Willis & Pryor | Willis & Pryor | | TEC | |
|---|---|---|---|---|---|---|
| | $B_M^{static}$ (Å$^2$) | $B_M^{static}$ (Å$^2$) | $T_D$ (K) | | $T_D$ (K) | |
| Sample–conditions | $T \leq 298$ K | $T \leq 298$ K | $T \leq 298$ K | Average | $T \leq 298$ K | All $T$ range |
| LWO_**P**-dry(Ar)$^{ILL}$ | 0.41 (17) (Fig. 4) | 0.55 (2) | 354 (19) | 348 (9) | 462 (26) | 580 (33) |
| LWO_**P**-$D_2O$(Ar)$^{ILL}$ | 0.38 (12) | 0.51 (2) | 358 (21) | | | |
| LWO_**P**-$D_2O$(SA)$^{SINQ}$ | 0.41 (12) | 0.48 (1) | 343 (11) | | | |
| Re20-dry(Ar)$^{ILL}$ | 0.41 (14) | 0.48 (1) | 361 (10) | 359 (7) | 438 (19) | 571 (45) |
| Re20-$D_2O$(Ar)$^{ILL}$ | 0.42 (11) | 0.47 (2) | 343 (13) | | | |
| Re20-$D_2O$(SA)$^{SINQ}$ | 0.30 (11) | 0.36 (2) | 383 (17) | | | |

number of vacant sites in the unit cell in wet($D_2O$) specimens compared to the dry(Ar) pre-treated specimens may be linked to higher structural stability. As different pre-treatments yield different oxidation states, the reduced Re atoms are expected to increase the static disorder. The measurements done at the optimum wavelength ($\lambda$ = 1.798 Å) at the FIREPOD diffractometer at the BERII reactor allow us to refine consistently only the isotropic displacement parameters owing to the lack of high-angle data and only medium resolution. Hence, a fit according to the Willis & Pryor (1975) approach including all data points shown in Fig. 8 for LWO_**P** and Re20 could not be performed. Good agreement is achieved between the approaches of Willis & Pryor (1975) and Housley & Hess (1966) for $T \leq 298$ K (see Table 5).

Moreover, the values for $B_M^{static}(T = 0\,K)$ indicate that the structural model used to fit Re20 is as good as that used to fit LWO_**P**. In order to estimate the average static disorder, the values obtained from the Willis & Pryor (1975) approach were transformed into average r.m.s. displacements, as calculated previously for LWO_**P**-dry(Ar) [0.07 (4) Å, see Fig. 4]. The Willis & Pryor (1975) approach is more accurate than that of Housley & Hess (1966) and gives for LWO_**P**-dry(Ar)/wet($D_2O$) specimens average r.m.s. values of 0.08 (2) Å. Likewise, average r.m.s. values of 0.07–0.08 (2) Å for Re20 specimens were determined. Hence, as for sample LWO_**P**, the calculated r.m.s. values for Re20 are too low to further improve the structural model. This conclusion, however, excludes the detailed modelling of anion librations reported in the literature or anharmonic vibration of the anions in LWO, presented below.

In order to obtain a second value of $T_D$ to compare with the $T_D$ extracted from the Willis & Pryor (1975) fit, an analysis of the thermal expansion of Re20 and LWO_**P** was performed. Moreover, in this section an explanation for using the approximation on the Grüneisen relation (see §3.1) will be provided. The linear thermal expansion coefficient, $\alpha_L = (1/L_0)(dL/dT)$, where $L$ is the sample length and $L_0$ the sample reference length, was calculated according to the refined cell parameters $a$ (Fig. 2) with $L = a$. Finally, the calculated data of $\alpha_L$ were fitted with the Debye model, according to the following equation:

$$\alpha_L = \alpha_0 \left(\frac{T}{T_D}\right)^3 \int_0^{T_D/T} \frac{y^4 \exp(y)}{[\exp(y) - 1]^2}\, dy, \qquad (11)$$

where $\alpha_0$ is a temperature-independent fitting parameter.

Approximations were made for some parameters used in the Grüneisen relation $c_v\gamma = k\alpha_V$, where $c_v$, $\gamma$, $k$ and $\alpha_V$ are, respectively, the specific heat, Grüneisen parameter, bulk modulus and volumetric expansion. As $k$ and $\gamma$ are usually only weakly dependent on the temperature, the thermal expansion coefficient $\alpha_V$ and the specific heat $c_v$ exhibit about the same temperature dependence. For any cubic structure, the volumetric expansion then becomes $\alpha_V = 3\alpha_L$. The Debye model can hence be applied to the present ND data to deduce the thermal expansion. Furthermore, from a simple integration in $dT$ of the first and the last terms of the following equations,

$$\frac{1}{a_0}\frac{da}{dT}\alpha_L \cong c_v \propto T^3 \qquad (T \ll T_D), \qquad (12)$$

$$\frac{1}{a_0}\frac{da}{dT}\alpha_L \cong c_v = \text{constant} \qquad (T > T_D), \qquad (13)$$

it can be inferred that the behaviour of the cell parameter as a function of temperature $a(T)$ can be described as $a(T) = A + BT^4$ and $a(T) = HT$ (with $A$, $B$ and $H$ constants) for $T << T_D$ and $T > T_D$, respectively, as shown in Fig. 2.

The linear thermal expansion coefficient $\alpha_L$ is in the following referred to as the thermal expansion coefficient (TEC). The TECs determined using the ND data of LWO_**P** and Re20 with the respective fits [equation (11)] are shown in Fig. 9. To improve the statistics, all measurements of thermal expansion for one and the same specimen were combined, irrespective of their specific treatment, *i.e.* it was assumed that the TEC is independent of the specific treatment (Seeger *et al.*, 2013).

The TEC values at high temperatures are close to but not identical to those obtained from dilatometry measurements reported in the literature (Fig. 9, red dotted and green dash–dotted lines; Seeger *et al.*, 2013). This discrepancy could be due to differences in sample stoichiometry, to small temperature

offsets during the experiment at BERII performed at high temperatures or to the creation of thermal vacancies (Simmons & Balluffi, 1960). The latter, however, is not expected, as the specimens were investigated in a temperature range still far away from the $La_6WO_{12}$ melting temperature [2323 (20) K] reported in the literature (Chang & Phillips, 1964).

A comparison of the $T_D$ values obtained from the TECs (Fig. 9) and those extracted from the Willis & Pryor (1975) approach is also presented in Table 5. The average values of $T_D$ derived from the thermal expansion coefficients [equation (11)] for LWO_**P** and Re20 in the temperature region $T \leq 298$ K are comparable to each other. However, the $T_D$ values extracted from the TECs do not match with the ones obtained from the Willis & Pryor (1975) approach (Table 5) for the same temperature range, being on average larger by about 22%. The reason for the large variation in $T_D$ might be related to the restricted temperature range of ADP data points in the high-temperature region ($T > T_D$) and/or data which cannot be used to fit $T_D$ through the Willis & Pryor (1975) approach. As a rule of thumb, the Debye temperature values established with equation (10) in Fig. 8 depend on the slope of the interpolation curve for high temperatures: the steeper the slope, the lower $T_D$. A comparable discrepancy has been reported for cubic yttria-stabilized zirconia (YSZ), which has a structure (fluorite $Fm\bar{3}m$) similar to the LWO and LW(Re)O samples treated here. Argyriou (1994) reported for YSZ a Debye temperature $T_D = 533$ (20) K, fitted with equation (10) in a temperature range of $5 \leq T \leq 1323$ K. In contrast, the best fit of $T_D$ in YSZ of Erich & Ma (1998) yielded $T_D = 963$ K in the range $4 \leq T \leq 1923$ K. The latter authors, however, added an anharmonic term to equation (10), suggesting that the harmonic approximation applied to thermal displacement parameters [from which equation (10) is derived] does not hold for disordered structures with anionic defects as in YSZ.

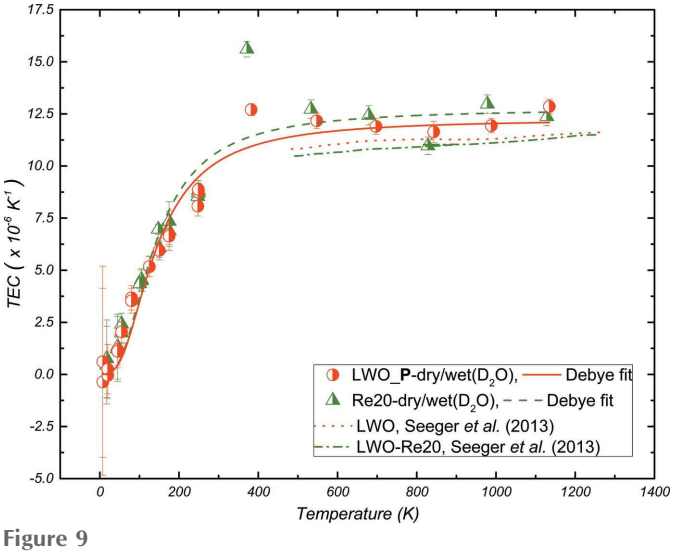


**Figure 9**
Linear thermal expansion coefficient TEC as a function of the temperature, for samples LWO_**P** and Re20. All different pre-treatments are contained in the same datasets. Fits were performed with equation (11) and the results are reported in Table 5.

As the LWO structure is related to YSZ, being also disordered and containing oxygen vacancies, it can be inferred that LWO could also undergo cubic anharmonic vibration of the anions as reported for perfect fluorite structures in the work of Willis & Pryor (1975). Following the YSZ example, anharmonic and harmonic interpolations of $W_1$, $O_1$ and $O_2$ equivalent displacement parameter values ($B_{eq}$) for LWO have been performed. Non-negligible anharmonic vibrations of the anions occupying the 96*k* Wyckoff sites, not present for the $O_2$ and $W_1$ atoms, have been found. Details of the study on anharmonic vibrations of the LWO system are reported in the supporting information (Fig. S7).

## 4. Summary and conclusions

In this work, the structure, chemical composition and thermal expansion of lanthanum tungstates and Re-substitited lanthanum tungstates ($La_{5.4}W_{1-y}Re_yO_{12-\delta}$, $0 \leq y \leq 0.2$) were investigated using thermogravimetry, electron probe microanalysis and neutron diffraction. A phase diagram of Re-substituted LWO is reported, where a shift of the single-phase region to higher La/(W + Re) ratios with increasing Re concentration is found. Provided that W evaporation is taken into account, preparation of LW(Re)O specimens must conform to the single-phase region determined in the present work. Increasing the Re substitution in LWO leads to lower water uptake at equal La/(W + Re) ratio. The difference observed in water uptake of LWO_**P** and Re20 is ascribed to the +7 oxidation state of Re atoms in an oxidized state occupying the 48*h* Wyckoff site. The 48*h* Wyckoff site is responsible for the charge compensation in LWO: replacement of $W^{6+}$ by $Re^{7+}$ decreases the oxygen vacancy concentration in the unit cell. This result is corroborated by Rietveld refinements: the oxygen vacancies sit on the 32*f* Wyckoff site, bonded to the 48*h* site responsible for charge compensation. Rietveld refinements give larger SOFs for the 32*f* Wyckoff site occupied by oxygen atoms in $D_2O$ conditions compared to dry conditions for both nonsubstituted LWO (LWO_**P**) and Re-substituted LWO (Re20). Moreover, Rietveld refinement results show that the 4*a* Wyckoff site has the same coordination number ($N \simeq 6$) independently of Re substitution and of dry/wet conditions. That Re substitutes for W statistically on 4*a* and 48*h* Wyckoff sites ($Fm\bar{3}m$ space group) has also been inferred independently by combining EPMA and the average scattering lengths at the cation positions obtained from ND. In addition, Rietveld refinements suggested that the model of Scherb (2011) with a split 48*h* site describes the structure of LWO_**P** as well as that of Re20 more satisfactorily than the model of Magraso *et al.* (2013). The structure of wet($D_2O$) materials was found to be slightly less disordered than that of the materials pre-treated in dry argon atmosphere. This fact was ascribed to a higher concentration of vacant sites in the unit cell for LWO_**P** and also to Re reduction in Re20. Such reasons explain why refinements of wet($D_2O$) specimens were found to be more stable than those of the dry(Ar) samples, for Re-substituted specimens. The conclusion that follows is that refinements on specimens pre-treated in oxidizing conditions

reach better convergence and thus can be refined with a higher number of free parameters. The lattice parameter follows satisfactorily the Debye model at low [$a(T) = A + BT^4$] and high [$a(T) = HT$] temperatures for LWO_**P** and Re20. Using the approach of Willis & Pryor (1975) the Debye temperatures have been estimated for LWO_**P** and Re20 and compared with those extracted from thermal expansion coefficients. However, the Debye temperature estimated through the Willis & Pryor approach is too low, as a result of anion anharmonic displacements already found in disordered fluorite structures such as YSZ. Therefore, the Debye temperatures extracted from the thermal expansion coefficients seem to be more reliable, being $T_D$ = 580 (33) K and $T_D$ = 571 (45) K for LWO_**P** and Re20, respectively. Anion anharmonic displacements are proved to exist in the LWO system for the first time. An understanding of the role of such anion anharmonic vibrations together with the reported anion libration movements around W (Magraso *et al.*, 2013) can give further insights into the structural details, allowing room for improvement of the present LWO crystal structure.

## Acknowledgements

We thank the Institute Laue–Langevin, the Paul Scherrer Institute and the Helmholtz-Zentrum Berlin for the provision of beamtime and the beamline scientists E. Suard (D2B), V. Pomjakushin (HRPT) and A. Hoser (FIREPOD) for their help during the experiments. We thank also J. Nissen (TU Berlin) for conducting the EPMA measurements and C. Leistner and C. Förster (HZB) for help in performing TG and XRD experiments and in sample preparation. The Helmholtz Association funded this work through the Helmholtz Alliance MEM-BRAIN (Initiative and Networking Fund).

## References

Amsif, M., Magrasó, A., Marrero-López, D., Ruiz-Morales, J. C., Canales-Vázquez, J. & Núñez, P. (2012). *Chem. Mater.* **24**, 3868–3877.
Argyriou, D. N. (1994). *J. Appl. Cryst.* **27**, 155–158.
Bruker (2008). *Diffracplus Evaluation Package EVA 14*. Release 15 July 2008. Bruker AXS GmbH, Karlsruhe, Germany.
Chambrier, M. H., Ibberson, R. M. & Goutenoire, F. (2010). *J. Solid State Chem.* **183**, 1297–1302.
Chang, L. L. Y. & Phillips, B. (1964). *Inorg. Chem.* **3**, 1792–1794.
Chang, L. L. Y., Scroger, M. G. & Phillips, B. (1966). *J. Inorg. Nucl. Chem.* **28**, 1179–1184.
Cheary, R. W. (1991). *Acta Cryst.* B**47**, 325–333.
Chizmeshya, A. V. G., Bauer, M. R. & Kouvetakis, J. (2003). *Chem. Mater.* **15**, 2511–2519.
Erdal, S., Kalland, L. E., Hancke, R., Polfus, J., Haugsrud, R., Norby, T. & Magrasó, A. (2012). *Int. J. Hydrogen Energy*, **37**, 8051–8055.
Erich, K. & Ma, Y. (1998). *J. Phys. Condens. Matter*, **10**, 3823.
Escolastico, S., Seeger, J., Roitsch, S., Ivanova, M., Meulenberg, W. A. & Serra, J. M. (2013). *ChemSusChem*, **6**, 1523–1532.
Escolástico, S., Solís, C., Scherb, T., Schumacher, G. & Serra, J. M. (2013). *J. Membr. Sci.* **444**, 276–284.
Escolástico, S., Solís, C. & Serra, J. M. (2012). *Solid State Ionics*, **216**, 31–35.
Escolástico, S., Somacescu, S. & Serra, J. M. (2014). *Chem. Mater.* **26**, 982–992.
Evans, J. S. O. (2010). *Mater. Sci. Forum*, **651**, 1–9.
Fischer, P., Frey, G., Koch, M., Könnecke, M., Pomjakushin, V., Schefer, J., Thut, R., Schlumpf, N., Bürge, R., Greuter, U., Bondt, S. & Berruyer, E. (2000). *Phys. B Condens. Matter*, **276–278**, 146–147.
Fischer, R. X. & Tillmanns, E. (1988). *Acta Cryst.* C**44**, 775–776.
Furrer, A., Mesot, J. & Strässle, T. (2009). *Neutron Scattering in Condensed Matter Physics.* London: World Scientific.
Ganguly, P., Shah, N., Phadke, M., Ramaswamy, V. & Mulla, I. S. (1993). *Phys. Rev. B Condens. Matter*, **47**, 991–995.
Genovese, A., Contrisciani, N., Ortenzi, F. & Cazzola, V. (2011). *Int. J. Hydrogen Energy*, **36**, 1775–1783.
Hancke, R., Li, Z. & Haugsrud, R. (2012). *Int. J. Hydrogen Energy*, **37**, 8043–8050.
Hancke, R., Magrasó, A., Norby, T. & Haugsrud, R. (2013). *Solid State Ionics*, **231**, 25–29.
Haugsrud, R. (2007). *Solid State Ionics*, **178**, 555–560.
Haugsrud, R., Larring, Y. & Norby, T. (2005). *Solid State Ionics*, **176**, 2957–2961.
Haugsrud, R. & Norby, T. (2006). *Nat. Mater.* **5**, 193–196.
Hewat, A. W. & Heathman, S. (1984). *Acta Cryst.* A**40**, C364.
Hill, R. J. & Cranswick, L. M. D. (1994). *J. Appl. Cryst.* **27**, 802–844.
Ho, T. & Karri, V. (2011). *Int. J. Hydrogen Energy*, **36**, 10065–10079.
Holt, D. van, Forster, E., Ivanova, M. E., Meulenberg, W. A., Müller, M., Baumann, S. & Vassen, R. (2014). *J. Eur. Ceram. Soc.* **34**, 2381–2389.
Housley, R. M. & Hess, F. (1966). *Phys. Rev.* **146**, 517–526.
Ivanova, M. E., Meulenberg, W. A., Palisaitis, J., Sebold, D., Solís, C., Ziegner, M., Serra, J. M., Mayer, J., Hänsel, M. & Guillon, O. (2015). *J. Eur. Ceram. Soc.* **35**, 1239–1253.
Ivanova, M., Ricote, S., Meulenberg, W. A., Haugsrud, R. & Ziegner, M. (2012). *Solid State Ionics*, **213**, 45–52.
Ivanova, M. E., Seeger, J., Serra, J. M., Solis, C., Meulenberg, W. A., Fischer, W., Roitsch, S. & Buchkremer, H. P. (2012). *Chem. Mater. Res.* **2**, 56–81.
Iwahara, H. (1988). *J. Electrochem. Soc.* **135**, 529–533.
Iwahara, H., Esaka, T., Uchida, H. & Maeda, N. (1981). *Solid State Ionics*, **3–4**, 359–363.
Jacob, K. T., Raj, S. & Rannesh, L. (2007). *Int. J. Mater. Res.* **98**, 776–779.
Kalland, L.-E., Magrasó, A., Mancini, A., Tealdi, C. & Malavasi, L. (2013). *Chem. Mater.* **25**, 2378–2384.
Kim, M., Sohn, Y.-J., Cho, C.-W., Lee, W.-Y. & Kim, C.-S. (2008). *J. Power Sources*, **176**, 529–533.
Larson, A. C. & Dreele, R. B. V. (2004). Report LAUR 86–748. Los Alamos National Laboratory, New Mexico, USA.
Li, W., Pessa, M. & Likonen, J. (2001). *Appl. Phys. Lett.* **78**, 2864–2866.
Magraso, A. & Frontera, C. (2016). *Dalton Trans.* **45**, 3791–3797.
Magrasó, A., Frontera, C., Marrero-López, D. & Núñez, P. (2009). *Dalton Trans.* **38**, 10273–10283.
Magrasó, A. & Haugsrud, R. (2014). *J. Mater. Chem. A*, **2**, 12630–12641.
Magraso, A., Hervoches, C. H., Ahmed, I., Hull, S., Nordstrom, J., Skilbred, A. W. B. & Haugsrud, R. (2013). *Mater. Chem. A*, **1**, 3774–3782.
Magrasó, A., Polfus, J. M., Frontera, C., Canales-Vázquez, J., Kalland, L. E., Hervoches, C. H., Erdal, S., Hancke, R., Islam, M. S., Norby, T. & Haugsrud, R. (2012). *J. Mater. Chem.* **22**, 1762–1764.
Massa, W. (2004). *Crystal Structure Determination.* Berlin, Heidelberg: Springer-Verlag.
Meulenberg, W. A., Ivanova, M., Buchkremer, H. P., Stöver, D., Alfaro, J. M. S. & Escolástico, S. (2013). Patent DE 102010027645 A1.
Murphy, S. T., Chroneos, A., Jiang, C., Schwingenschlogl, U. & Grimes, R. W. (2010). *Phys. Rev. B*, **82**, 073201.
Niknam, T., Bornapour, M. & Gheisari, A. (2013). *Energy Convers. Manage.* **66**, 11–25.
Norby, T. (1999). *Solid State Ionics*, **125**, 1–11.

Palisaitis, J., Ivanova, M. E., Meulenberg, W. A., Guillon, O. & Mayer, J. (2015). *J. Eur. Ceram. Soc.* **35**, 1517–1525.
Pechini, M. P. (1967). US Patent 3 330 697 A.
Rey, J. F. Q. & Muccillo, E. N. S. (2004). *J. Eur. Ceram. Soc.* **24**, 1287–1290.
Richard, D., Ferrand, M. & Kearley, G. J. (1996). *J. Neutron Res.* **4**, 33–39.
Scherb, T. (2011). PhD thesis, Technische Universität Berlin, Germany.
Scherb, T., Kimber, S. A. J., Stephan, C., Henry, P. F., Schumacher, G., Escolástico, S., Serra, J. M., Seeger, J., Just, J., Hill, A. H. & Banhart, J. (2016). *J. Appl. Cryst.* **49**, 997–1008.
Schiller, G. (1986). Thesis, Dreieck Verlag Löchner, Bochum, Germany.
Schulze-Küppers, F., ten Donkelaar, S. F. P., Baumann, S., Prigorodov, P., Sohn, Y. J., Bouwmeester, H. J. M., Meulenberg, W. A. & Guillon, O. (2015). *Sep. Purif. Technol.* **147**, 414–421.
Seeger, J., Ivanova, M. E., Meulenberg, W. A., Sebold, D., Stöver, D., Scherb, T., Schumacher, G., Escolástico, S., Solís, C. & Serra, J. M. (2013). *Inorg. Chem.* **52**, 10375–10386.
Shannon, R. D. (1976). *Acta Cryst.* A**32**, 751–767.
Shimura, T., Komori, M. & Iwahara, H. (1996). *Solid State Ionics*, **86–88**, 685–689.
Simmons, R. O. & Balluffi, R. W. (1960). *Phys. Rev.* **117**, 52–61.
Sorensen, B. (2007). *Int. J. Hydrogen Energy*, **32**, 1597–1604.
Stephan, C., Schorr, S., Tovar, M. & Schock, H. W. (2011). *Appl. Phys. Lett.* **98**, 091906.
Su, S.-J., Cheng, B.-W., Xue, C.-L., Zhang, D.-L., Zhang, G.-Z. & Wang, Q.-M. (2012). *Acta Phys. Sinica*, **61**, 176104.
Tobbens, D. M., Stusser, N., Knorr, K., Mayer, H. M. & Lampert, G. (2001). *Epdic 7: European Powder Diffraction*, Parts 1 and 2, edited by R. Delhez & E. J. Mittemeijer, pp. 288–293. Switzerland: Trans Tech Publications.
Vegard, L. (1921). *Z. Phys.* **5**, 17–26.
Wang, D., Chen, S., Xu, C. & Xiang, W. (2013). *Int. J. Hydrogen Energy*, **38**, 5389–5400.
Willis, B. T. M. & Pryor, A. W. (1975). *Thermal Vibrations in Crystallography*. Cambridge University Press.
Yoshimura, M. & Rouanet, A. (1976). *Mater. Res. Bull.* **11**, 151–158.